

ABSTRACT

Development of a Digital Optical Diagnostic System for the CASPER GEC rf Reference Cell

by Carolyn M. Boessé

Thesis Chairperson: Truell W. Hyde II, Ph.D.

The development and implementation of a completely digital optical analysis system for dusty plasma research has been completed. This system minimizes data loss during acquisition and processing and allows image data to be acquired much more quickly and efficiently than in previous analog methods. The automated camera-lens system has been shown to be successful in imaging plasma discharge regions at a sufficient acquisition rate with multiple images to provide ease of analysis concerning position and velocity of particles and ordering of the crystal lattice. Analysis techniques have been improved due primarily to uncompromised raw data with Matlab providing a unique analysis toolset for processing data via PIV and PTV algorithms. PIV algorithms have been shown to have the advantage of greatly reducing computation time and the ability to calculate particle velocities when individual particles are not resolvable, while PTV algorithms provide more specific information about dust grain interactions and more precise velocity calculations.

Development of a Digital Optical Diagnostic System
for the
CASPER GEC rf Reference Cell

by

Carolyn M. Boessé, B.S.

A Thesis

Approved by the Department of Physics



Bennie F.L. Ward, Ph.D., Chairperson

Submitted to the Graduate Faculty of
Baylor University in Partial Fulfillment of the
Requirements for the Degree
of
Master of Science

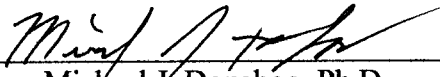
Approved by the Thesis Committee



Truell W. Hyde II, Ph.D., Chairperson

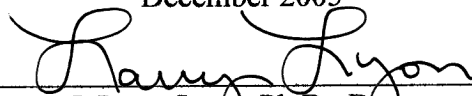


Dwight P. Russell, Ph.D.



Michael J. Donahoo, Ph.D.

Accepted by the Graduate School
December 2005



J. Larry Lyon, Ph.D., Dean

Copyright © 2005 by Carolyn M. Boessé

All rights reserved

TABLE OF CONTENTS

List of Figures	Page iv
List of Tables	v
1. Introduction and Background	1
1.1 Purpose.....	1
1.2 Astrophysical Dusty Plasmas.....	2
1.3 Industrial Dusty Plasmas.....	5
1.4 Thesis Layout.....	8
2. Constituents of Complex Dusty Plasmas	9
2.1 Dusty Plasmas.....	9
2.2 Grain Charging.....	9
2.3 Coulomb Lattice Structure.....	14
2.4 Measuring Order of a Crystal Lattice	16
2.4.1 Voronoi Diagram	17
2.4.2 Pair Correlation Functions	18
3. GEC Reference Cell and Plasma Crystals	22
3.1 GEC Reference Cell.....	22
3.2 Reference Cell Design	23
3.3 CAPER Reference Cell.....	27
3.4 Plasma Crystals.....	29
4. Research and Methodology.....	35
4.1 Optical System Development	35
4.1.1 Cell Dimensions.....	36
4.1.2 Dust Cloud Paramters	38
4.1.3 Image Capture Rate.....	39
4.1.4 Laser Illumination.....	40
4.2 Image Capture and Storage.....	41
4.3 Processing of Image Data	42
5. Results.....	48
5.1 Software Validation	48
5.2 Optical System Validation	51
6. Discussion and Conclusions	58
Appendix A	60
Bibliography	80

LIST OF FIGURES

Figure	Page
1 Saturn's F-Ring taken from Cassini	4
2 Saturn's A and B bands taken from Cassini	4
3 Great Nebula in Orion taken from Hubble Space Telescope	6
4 Close-up of proplyds in Orion Nebula taken from Hubble Space Telescope	6
5 Two-dimensional crystal lattice (Pieper, 1996)	17
6 Voronoi diagram (Pieper, 1996)	18
7 Pair-correlation function for a two-dimensional crystal (Melzer, 1996)	19
8a Pair-correlation function of a liquid	20
8b Pair-correlation function of a gas	20
9 Bond-orientation correlation function (Pieper, 1996)	21
10 Main vacuum chamber of GEC rf reference cell (Olthoff, 1995)	24
11 Schematic cross-section of GEC rf reference cell (Olthoff, 1995)	24
12 L-C schematic diagram (Hargis, 1994)	26
13 Simplified l-C equivalent circuit (Hargis, 1994)	27
14 CASPER rf reference cell	29
15 Two-dimensional horizontal hexagonal lattice structure (Morfill, 1996)	32
16 Vertical slice of crystal (Morfill, 1996)	32
17 Horizontal slice of hexagonal lattice (Chu, 1994)	33
18 CASPER GEC rf reference cell and optical system	39
19 Laser illumination apparatus schematic (Thomas, 1994)	40
20 Unfiltered digital image of dusty plasma	41
21 Black and white image of 9 μm dust	43
22a Pair-correlation function	44
22b Voronoi diagram	44
23a PTV velocity vector plot	46
23b PIV velocity vector plot	46
24 Particle cloud of 7 μm spheres (Thomas, 1994)	49
25 Voronoi diagram of particles in Figure 24 (Thomas, 1994)	49
26 <i>GrainiacI</i> Voronoi diagram of particles in Figure 24	50
27 <i>GrainiacI</i> pair-correlation function of particles in Figure 24	51
28 Data image of horizontal layer of 9 μm melamine formaldehyde spheres	52
29 Particle position plot	55
30 Velocity vector plot	55
31 Velocity distribution plot	56
32 Voronoi diagram	57
33 Pair-correlation plot	57

LIST OF TABLES

Table		Page
1	CASPER GEC rf reference cell operating parameters	53

ACKNOWLEDGMENTS

I would like to thank Dr. Truell Hyde for all his guidance and encouragement and Dr. Lorin Matthews for her extensive input and editing. I would also like to thank my committee members, Dr. Dwight Russell and Dr. Jeff Donahoo for their input on this thesis. My deepest gratitude and those most deserving of praise are the guys of CASPER at TSTC: Jerry Reay, Mike Cook, Jimmy Schmoke, and all of the students over the past few years.

CHAPTER ONE

Introduction and Background

1.1 Purpose

This project developed from a need to provide an effective means of acquiring and processing digital images of a Coulomb crystal formed within a complex plasma produced in a rf reference cell. The purpose of this project was threefold: (1) to develop a digital optical capture system utilizing charge-coupled device (CCD) technology; (2) provide analysis and sequencing for a series of two-dimensional images; and (3) develop particle tracking velocimetry (PTV) and particle imaging velocimetry (PIV) programs.

Observing the liquid and/or crystalline phases of a complex plasma and then collecting the necessary data becomes somewhat problematic for an experimental complex dusty plasma. Once dust is introduced into the plasma, any perturbation from physical probes or other instruments will change the parameters of the system (Pieper, 1996b). Thus, the only way to collect data without perturbing the dusty plasma is optically.

The advent of high-speed computing has recently led to the use of charge-coupled device (CCD) cameras interfaced to a desktop computer to capture and process such optical data. By imaging the plasma over a period of time, many of the required observations and measurements can be made. A computer program starts the image collection and time stamps each image with the acquisition time in order to sequence images for later processing. Analysis continues by removing noise from the image through digital dynamic filtering. Particle positions can then be determined through a second algorithm involving a radially sweeping pattern which finds the closest neighbor between

frames. Individual particles are then able to be tracked between frames and their velocities determined. Additional quantities of interest that may be determined include, but are not limited to, the Debye length, charge coupling ratio, interparticle spacing, layer spacing, pair-correlation function, Voronoi diagrams, and particle density (Boessé et al, 2002). All of these measurements and parameters characterize the dusty plasma and can be determined optically without disturbing the complex dusty plasma.

Obtaining and analyzing data from the reference cell without perturbing the plasma requires an efficient optical diagnostic system. Recent technological advances in CCD camera systems have provided an ideal tool for optical diagnostics versus past performance employing analog optical systems. Since analog images must first be converted to a digital format before analysis, an undetermined amount of data may be lost from each frame. However, CCD camera systems capture images in a digital format that may be directly exported for analysis without this loss of data due to digitizing.

Image analysis of the dusty plasma can employ both the particle tracking velocimetry (PTV) and particle image velocimetry (PIV) techniques. PTV algorithms are designed to track individual particles from image frame to frame, comparing relative positions. PIV allows for particle velocities, pair correlation functions, and thermal energy of the plasma to also be determined.

1.2 Astrophysical Dusty Plasmas

Naturally occurring astrophysical dusty plasmas such as those found in planetary rings, cometary tails, interstellar clouds and nebulae, and interplanetary and planetary formations were the catalyst topics of interest for research in dusty plasmas. Although there is no evidence yet, astrophysical dust is believed to be predominantly composed of

various ices, oxides, graphites, and other carbon-rich materials (Bowers, 1984; Sandford, 1996). The dynamics of such small charged particles within solar system environments can be strongly influenced by electromagnetic forces. Dust particles adjust their charge in order to find a local equilibrium within the charging plasma while the electrostatic fields within the plasma and the particles contained within uniquely determine the shape and particle distribution (Horanyi, 1996).

Planetary rings display a form of dusty plasma in its weakest definition, with an example being Saturn's rings. These rings are primarily composed of solid particles but may also contain a plasma component (Goertz, 1989) with charged grains within the planetary magnetosphere subjected to electromagnetic as well as gravitational forces. Smaller dust grains will be more strongly influenced by the plasma and can often create unique particle distributions in the form of rings, while larger particles are primarily dominated by gravitational forces which eventually lead to orbital decay (Goertz, 1989). The E, F, and G rings of Saturn are predominately composed of particles in the 0.1-10 μm range (Taylor, 1992). Figures 1 and 2 show images from the Cassini Mission displaying Saturn's F-ring, A and B-rings and spokes. These particles interact with the plasma in a loosely coupled form where the particles are suspended in the plasma and may perhaps exhibit liquid crystal formation where a loosely ordered structure might be observed. Fluctuations within the plasma produce particle density gradients due to the continuously changing ion and electron currents.

Cometary tails are composed of dust and gases ejected from the comet itself. Some of the escaping dust becomes ionized and mixes with the ejected dust to form a dusty plasma system. Supposition has been made that some loosely ordered structures may exist

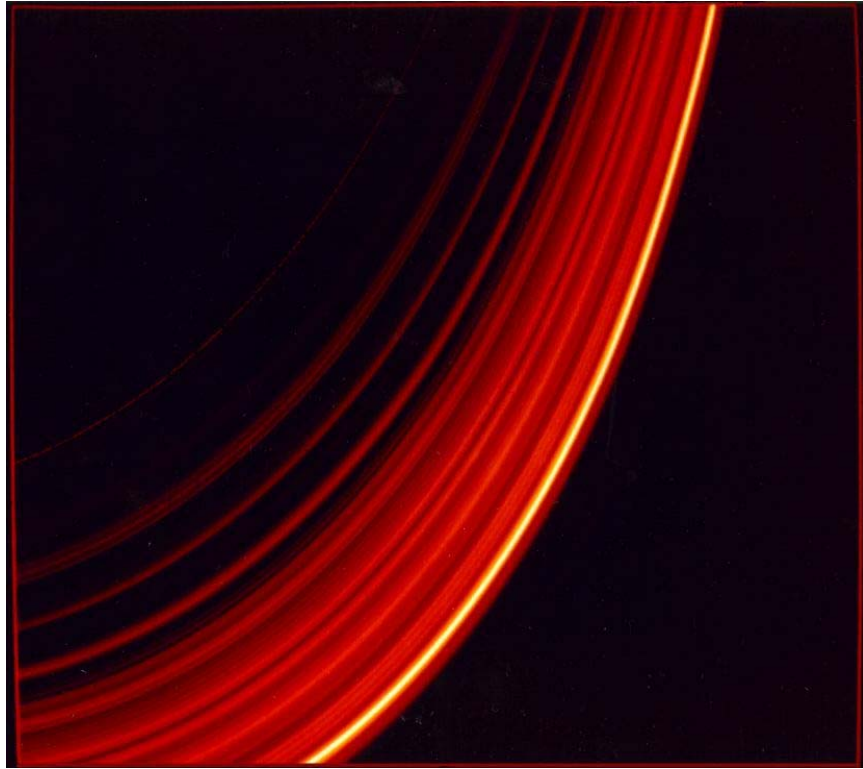


Figure 1. Image of Saturn's F-ring taken from Cassini.

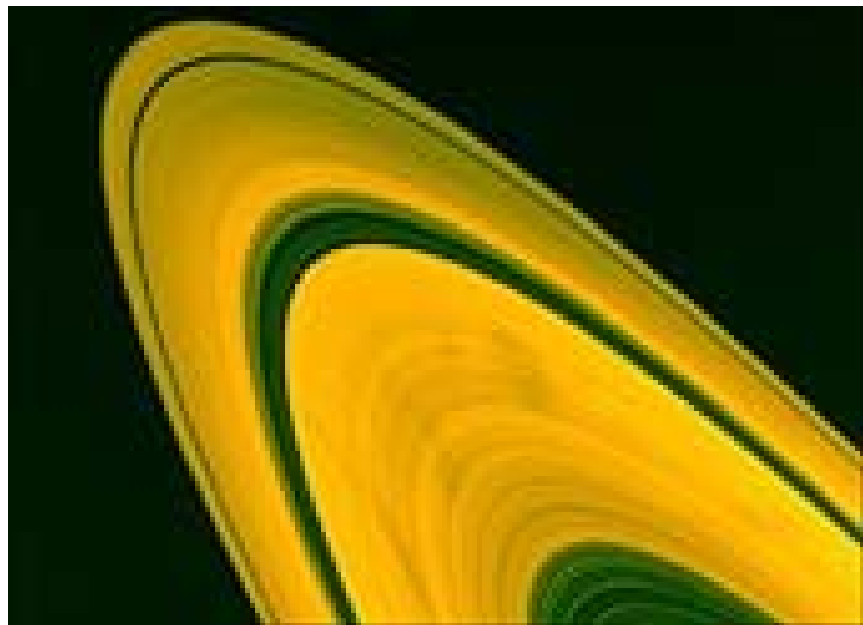


Figure 2. This color-enhanced image shows the dark spoke-like features in the rings. The spokes seem to form very rapidly with sharp edges and then dissipate. The A ring appears as the outermost bands but in this image appears as two bands divided by the Encke's division. The Cassini's division divides the A and B bands.

under these conditions as well (Serezhkin, 2000). This possibility is strengthened by the fact that gravity plays no important role in the motion of grains near comets. The primary influence for dust grain motion originates from radiation pressure, plasma drag, and electromagnetic forces. As such, cometary dust trails are shaped primarily by electromagnetic forces and grain size (Goertz, 1989).

One of the more interesting combinations of dust and gas occurs in interstellar clouds. Highly ionized gases with moderate amounts of dust can form denser areas where protostars may form (Lang, 1992). Nuclear reactions within these stars produce heavier elements which are then ejected in part by stellar winds or explosions in the form of novae or supernovae (Sandford, 1996). Stellar winds can also bring gas to these regions where ionization then occurs via photo-ionization (Bowers, 1984). Such dense areas are then largely dominated by gravitational forces versus electromagnetic forces creating first stars and then protoplanetary masses, planets, and subsequent ring structures (Goertz, 1989). In 1994 the Hubble Space Telescope took images of the Orion Nebulae which show proplyds, the beginning formations of solar systems. Figures 3 and 4 show the Orion Nebulae and a close-up of the proplyds.

1.3 Industrial Dusty Plasmas

Current semiconductor manufacturing relies heavily on a plasma etching processing technology. The two primary methods used are Reactive Ion Etching (Stoffels et al., 1998) and Plasma Enhanced Chemical Vapor Deposition (Bouchoule, 1999). Both methods place a carbon wafer in a plasma reaction chamber and then utilize the plasma to either deposit or remove material from the wafer's surface. During either process, dust is produced and can accumulate and then become suspended within the plasma sheath.

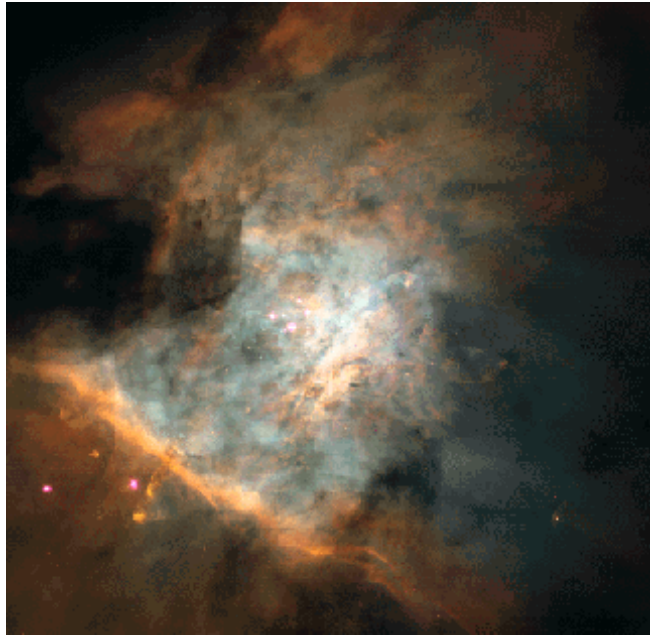


Figure 3. Image of the Great Nebula in Orion taken from the Hubble Space Telescope in 1994. The Orion Nebula contains many stellar nurseries including proplyds.



Figure 4. A close-up image of the proplyds in the Orion Nebulae. Proplyds are infant solar systems in the process of formation. This image was taken in 1994 by the Hubble Space Telescope.

Once the etching process is complete, the suspended dust particles drop to the surface of the wafer, contaminating it and often creating defects.

Such contamination has become a major problem in semiconductor manufacturing. A single dust particle deposited onto the wafer's surface can render a semiconductor chip useless (Jellum, 1991; Samsonov, 1999). One of the first attempts to rectify this problem involved conducting the manufacturing process in rooms designed to minimize outside sources of contamination. Such clean rooms helped to reduce the problem, but failed to solve the contamination problem in full due to the fact that (as explained above) contaminants are actually generated in the plasma etching or deposition process itself. Over the past decade, various methods for controlling the problem have been advanced. For example, a flow of neutral gas introduced into the etching chamber to 'blow' contaminants away from the semiconductors has been the most commonly used technique to minimize contamination (Bouchoule, 1999; Sheehan, 1990; Stoffels, 1998). Electrostatic forces have been used in a similar manner. Both of these methods work reasonably well either alone or in conjunction with one another, but neither is perfectly efficient. Clean rooms are not perfect and contaminants will invariably appear and 'blowing' contaminants away may introduce new electrostatic forces with the possibility of affecting the etching process itself. Thus, small particles may still be present in the plasma and act as contaminants. The presence of these remaining dust particles stimulated research into complex dusty plasmas in order to better understand dust dynamics within a plasma and control the suspension and deposition of the dust.

1.4 Thesis Layout

Chapter 2 will describe in detail the experimental formation of complex dusty plasmas and the specific parameters employed for producing such systems in a laboratory setting. Chapter 3 will discuss the conditions necessary to form plasma crystals in laboratory settings including the experimental platform for conducting such plasma experiments. Chapter 4 will address the common problems and proposed solutions for the development of an optical diagnostic system, image capture, and processing techniques. Results will be discussed in chapter 5 with conclusions and discussion to follow in Chapter 6.

CHAPTER TWO

Constituents of Complex Dusty Plasmas

2.1 Dusty Plasmas

The semi-conductor industry prompted research into complex plasmas due to its ever increasing need for a high level of precision in the manufacture of their product. Investigation into the etching process employed in the fabrication of microchips and the complex plasmas produced during this process brought dusty plasmas into the laboratory setting. Even so, laboratory dusty plasmas can serve as a physical model system for the study of both astrophysical and industrial dusty plasmas (Quinn, 1996). Dust grain charging, coulomb lattice structure, and measure of order are a few of the areas of interest in dusty plasmas that are of importance to research in planetary and ring formation as well as microelectronics production in the semiconductor industry.

2.2 Grain Charging

Electron and ion collecting currents are dependent upon the conditions within the plasma and the particles themselves. Not only are the size and shape of the dust grains of importance, but the relative motion of the grain with the plasma, the potential difference between the grain surface and surrounding plasma, and the electron and ion velocity distributions play vital roles in the charging of dust grains (Mendis, 1994). As the dust particles are much greater in mass compared to the ions and electrons, the velocity of the dust particles due to thermal energy is negligible compared to velocities of the ions and

electrons in the laboratory setting. For this reason, only dusty plasmas where the dust has negligible velocity will be discussed.

Complex dusty plasmas formed in a laboratory setting generally utilize a partially ionized neutral gas with embedded small particles of solid matter. These grains become charged due to collisions with ions and electrons. The simplest discussion of grain charging is for an isolated dust grain immersed in a plasma. The continuous flux of electrons and ions to the particles' surface leads to a net charge on the dust particle. The electron and ion currents are defined as

$$I_e = -\frac{4\pi a^2 n_e e}{(2\pi\beta_e m_e)^{1/2}} e^{e\beta_e \phi} \quad (1)$$

$$I_i = \frac{4\pi a^2 n_i Ze}{(2\pi\beta_i m_i)^{1/2}} (1 - \beta_i Ze\phi)$$

where a is the particle radius, e is the magnitude of the electron charge, Ze is the ion charge, $\beta = 1/kT$, m_e and m_i are the masses for the electrons and ions respectively, and ϕ is the negative potential of the grain.

Normally ions and electrons within the plasma tend to be at approximately the same temperature. Since kinetic energy, $KE = Tk_B$ where T is temperature in Kelvin and k_B is the Boltzman constant, both species of particles will have the same kinetic energy. However, the velocity of the electron is much higher because ions are significantly more massive than the electrons. Due to the much higher mobility of the electrons, the net charge on the dust particles is typically negative, provided photoemission and secondary electron emission are negligible (Thomas, 1994 and 2000). The dust grain reaches equilibrium within the plasma such that the potential of the particle must be negative so as to increase the ion flux and reduce the electron flux (Northrop, 1991). By setting the sum

of the currents to a negative grain found in (1) equal to each other the potential of the grain is determined from

$$e^{e\beta_e\phi} = \left(\frac{\beta_e m_e}{\beta_i m_i} \right)^{1/2} (1 - \beta_i Z e \phi) \quad (2)$$

It is clear that both charging currents depend on the size of grain and temperature of the plasma.

While secondary electron emission charging is negligible for larger sized grains, the charging process for small grains could become dominated by this charging mechanism (Mendis, 1994). In addition, photoemission currents depend on the properties of the grain and the grain surface potential.

A secondary electron current can be created when primary electrons carrying sufficient energy penetrate the dust grain such that some electrons produced by ionization leave the grain and become a net positive charge to the grain. The quantity of secondary electrons produced depends not only on the incoming primary electron energy but the size and composition of the grain (Barge, 1998). The secondary electron current is determined to be

$$I_{\text{sec}} = 3.7 \delta_m I_e = F_s \left(\frac{E_m}{4kT} \right) \quad (3)$$

with

$$F_5(x) = x^2 \int_0^\infty t^5 e^{[-(xt^2+t)]} dt \quad (4)$$

where E_m is the characteristic energy at which the release of secondary electrons peak which occurs generally at energies between 0.1 keV to 2keV. δ_m is a material constant which typically ranges between 0.5 and 3.0 and I_e is the electron current.

The third mechanism for dust particle charging is the photoemission current. This charging process occurs when electrons on dust particles are exposed to ultraviolet radiation causing the electrons to photoionize. The escaping photoelectrons create a positive current that is a function of the material properties of the dust particle. Still assuring a negative potential on the dust grain, the photoemission current to a grain with radius a is defined by Goertz (1989) and Horányi (1996) as

$$I_v = \pi a^2 f \eta \quad (5)$$

where f is the flux of photons energetic enough to ionize the electrons and η is the photoemission efficiency of the material (typically close to unity but tending toward 0.1 for dielectric materials). The case when the dust particle potential is positive generally creates a situation where the photoelectrons will not escape but instead fall back onto the grain.

In most laboratory plasmas, secondary electron and photoionization currents are negligible due to the relatively low plasma temperatures, which render few high energy electrons and a lack of photons with sufficient energy to ionize dust particles. Thus, the only currents considered in this work to play an important role in the charging of dust particles are the ion and electron currents.

As mentioned, charging currents are dependent upon the surface potential of the dust particles. The surface potential and the equilibrium charge are in the simplest case related by

$$\phi = \frac{Q}{C} \quad (6)$$

where Q is the charge on the dust particle and C is its capacitance. The capacitance of the grain will depend upon the material of the dust particle, the surrounding environment, and

the interparticle separation of the dust particles. For the case of an isolated particle in plasma, the capacitance is a function primarily of the Debye length and the particle radius where the Debye length, λ_D , is defined as the radius at which the grain appears neutrally charged due to the surrounding positive charges (de Angelis, 1991; Goertz, 1989). In most environments the particle radius is negligible compared to the Debye length and the capacitance can be defined as

$$C = 4\pi\epsilon_0 a \quad (7)$$

However, if the radius is similar to the Debye length, the capacitance as defined by Bliokh (1994) becomes

$$C = 4\pi\epsilon_0 e^{\left(\frac{-a}{\lambda_D}\right)} \quad (8)$$

For the case of multiple grains in plasma, often the charge on the various grains will not be uniform due to the size variation of the dust grains within the dust cloud. Individual particles will then have different equilibrium charges according to the preceding equations.

Due to the charge distribution in the cloud, the dominant form of interaction between grains in a plasma is generally the Coulomb force. In free space charged particles would display a normal $1/r$ potential; however, in a complex plasma the dust is surrounded by plasma with the particles experiencing a shielded Coulomb (Yukawa) potential, due to the shielding of the dust grains by the ions and electrons of the plasma. The non-normalized Yukawa potential in its simplest form is defined as

$$U_d = \frac{Q'Q''}{r} e^{\left(\frac{-r}{\lambda_D}\right)} \quad (9)$$

where r is the distance between grains and the Debye length is defined as in Jackson (1974) as

$$\lambda_D \sqrt{\frac{kT}{4\pi n e^2}} = 6.91 \left(\frac{T}{n} \right)^{1/2} \quad (10)$$

where T is the temperature in degrees Kelvin and n is the electron density in units of cm^{-3} .

2.3 Coulomb Lattice Structure

Considering the Coulomb force as the only interaction between dust particles, there are three types of dust arrangements in plasma. The first is dust immersed in plasma. This case, dust particles are basically isolated from each other having an average interparticle spacing greater than the Debye length ($a \ll \lambda_D \ll d$), and thus have very little interaction with one another, and subsequently very little effect on the non-local plasma.

The second type of dust arrangement in plasma consists of low dust particle density within a plasma characterized by Debye lengths that are typically larger than the interparticle spacing, $a \ll d \ll \lambda_D$ (Mendis and Rosenberg, 1994). In this situation, the electric potentials of the dust particles overlap and they can interact with one another, and in turn the plasma. However, there is generally not sufficient interaction between particles to create order within the system.

The third type of dust arrangement in plasma creates what is known as a colloidal plasma. In these types of complex plasmas, dust is the driving force behind the local dynamics of the plasma and can no longer be considered a contaminant but must be defined as an integral component of the plasma system. A colloidal plasma is defined as a plasma in which more momentum is lost in collisions between ions or electrons and dust particles than with other plasma components. Additionally it must satisfy

$$n_d e Z \geq 0.44 n_e \quad (11)$$

or

$$n_d eZ \geq 0.02 n_i \quad (12)$$

where n_d , n_e , and n_i are the number densities of the dust, electrons, and ions, respectively, and eZ is the net number of electronic charges carried by the dust grain (Morfill, 1996). The degree to which the plasma is coupled to the dust increases with the charge state of the ions. Within the realm of colloidal plasmas there are two types: loosely coupled and highly coupled plasmas. Most early work on plasma crystallization was performed assuming a One Component Plasma (OCP) (Thomas, 1994). An OCP is a pure ion plasma where the overall confinement is controlled by a fixed external field. The behavior of an OCP is characterized by the coupling parameter Γ which is defined as the ratio of the interparticle Coulomb potential energy to the thermal energy or

$$\Gamma = \frac{Q^2}{4\pi\epsilon_0 k_B T r} \quad (13)$$

where T is the particle temperature, k_B is the Boltzmann's constant, and r is the average interparticle separation. Monte Carlo simulations have demonstrated that a complex plasma with a Γ value of 172 will solidify into a crystalline state (Ichimaru, 1982). Typically however, plasmas with $\Gamma > 2$ are rare (strongly coupled) with most laboratory plasmas having $\Gamma < 1$ and considered to be weakly coupled.

A loosely coupled plasma is characterized by $\Gamma < 1$ and tends to remain in a gaseous state with little four-fold symmetry or ordering of the suspended particles within the plasma. Highly coupled plasmas have $\Gamma > 1$ and will tend toward the formation of a dust lattice or crystalline state. Solidification of such a complex plasma occurs at a value of $\Gamma > 170$ where it is said to condense (Morfill, 1999b).

Unlike ionic crystals where lattice points alternate in charge, a Coulomb crystal is most often constructed of like charged particles. The first to predict such a structure was

Eugene Wigner in 1934. Wigner hypothesized that particles of like charge could arrange themselves in such a lattice when these particles were confined and subject to a low temperature in order to minimize thermal motion (1934). Early work produced Wigner crystals in electrolytic solutions that were formed over a period of weeks and were difficult to image since they were optically thick (Kose, 1973). Crystalline structures produced in an electron gas were not observed until the early 1990's at the junctions of two metals (Goldman, 1990).

The conditions for the actual solidification of small particles in plasma into a Coulomb lattice were best defined by Ikezi (1986). He stated that when Γ exceeded a critical value of 170 a Coulomb lattice was formed. This was later confirmed by Morfill (1999b) when investigating plasma condensation. For $\Gamma < 1$, no lattice structures were predicted nor have they been observed. However, as Γ is increased lattice structures were predicted with Ikezi proposing that a Coulomb lattice would form at $\Gamma > 170$. As Γ further increased, Coulomb solidification was said to occur.

2.4 Measuring the Order of a Crystal Lattice

Measuring the order of a crystal lattice within plasma has largely been an exercise in visual estimation. Two types of ordering are often evaluated: short range and long range. Short range ordering occurs when the lattice structure only extends to a particle's nearest neighbors. Long range ordering occurs when the lattice structure extends beyond the particle's nearest neighbor to several orders of nearest neighbors. Of the two, long range ordering is preferable in a crystal lattice because of the high degree of order present throughout the plasma cloud. Two techniques for determining the amount of order present in a crystal lattice are the construction of Voronoi diagrams and pair-correlation functions.

Figure 5 shows an image of a two-dimensional hexagonal crystal lattice formed by dust particles in plasma.

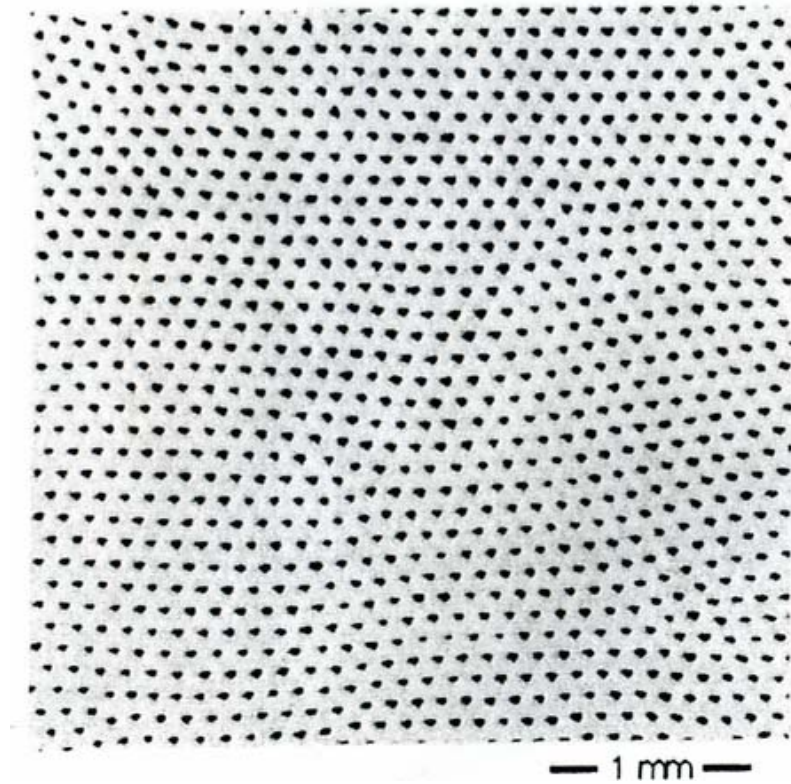


Figure 5. Image of a two-dimensional hexagonal crystal lattice of 9.4 μm -diameter polymer spheres in a plasma discharge (Pieper, 1996).

2.4.1 Voronoi Diagrams

Voronoi diagrams are constructed in order to create “cells” around individual particles. Cells are created by drawing the perpendicular bisector of the line joining two adjacent particles. These lines then intersect to form polygons around each particle. A perfect hexagonal crystal lattice will have all six-sided cells. Often there are a number of five and seven-sided cells in a Voronoi diagram which indicate defects in the overall crystal structure. A large number of these cells compared to six-sided cells indicates a low degree of order within the crystal lattice. A high ratio of the number of six-sided cells to

those of five and seven-sided cells indicates a high degree of order in the crystal lattice.

Figure 6 shows a Voronoi diagram with predominantly six-sided cells.

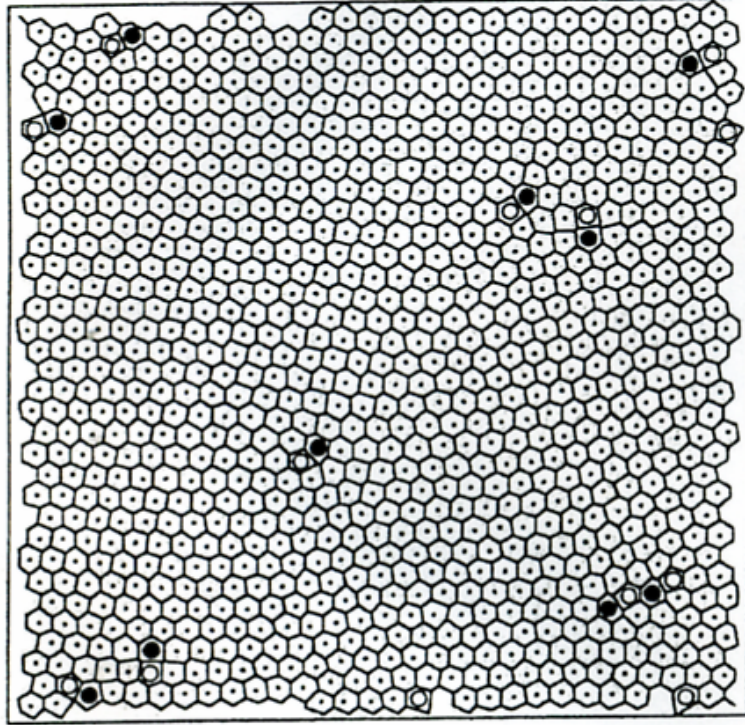


Figure 6. Voronoi diagram where each cell is labeled according to the number of nearest neighbors as follows: (○) five-sided, (•) six-sided, and (●) seven-sided (Pieper, 1996).

2.4.2 Pair Correlation Functions

There are two types of pair correlation functions used in conjunction with Voronoi diagrams to measure the degree of order within a crystal lattice. The first of these is often called the radial (pair) density distribution $g(r)$ which represents the probability of finding two particles separated by a distance r thus measuring the translational order in the structure (Quinn, 1995). To calculate $g(r)$ a particle is chosen as a center point with the number of particles then counted in concentric annular rings of radius r about this point. This number is then normalized by the annular ring's area and then averaged using each

particle as a center point. This yields $g(r)$ in units of areal density which is then normalized again by the average particle density so that the asymptotic value of $g(r)$ is unity. Figure 7 shows a typical graph of $g(r)$ for a single layer of a hexagonal lattice.

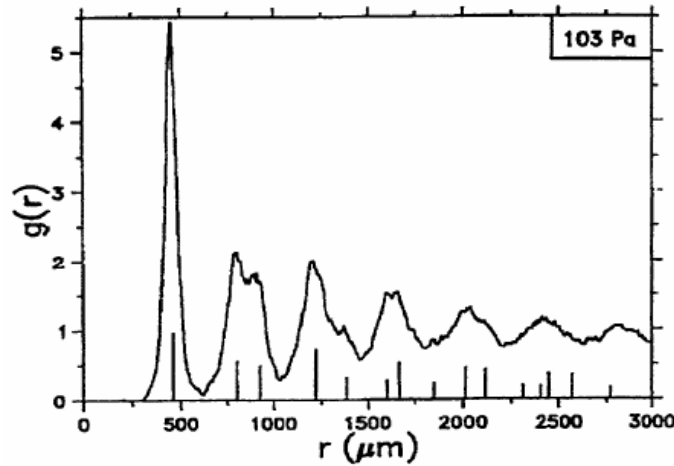


Figure 7. The pair correlation function $g(r)$ for a two-dimensional crystal. The vertical lines mark the position for an ideal hexagonal lattice (Melzer, 1996).

Clearly defined peaks within such a graph indicate a high degree of ordering to several times the nearest neighbor distance. When only one peak appears, short range order is indicated as is often found in liquid states (Figure 8a). When there is no clearly defined peak, there is no ordering present which is typical for a gaseous state (Figure 8b). Of these three, the first is preferable for this work since it indicates a long range, highly ordered crystal lattice.

The second type of correlation function is simply called the pair correlation function $g_6(r)$ and is defined in terms of the nearest neighbor bond angles of a lattice (Quinn, 1995). It measures the degree of orientation order based on the fact that bonds in a perfect crystal structure will all have the same angle of $\pi/3$ for a hexagonal lattice with respect to any arbitrary axis. To calculate $g_6(r)$ directly from the bonds a center point bond

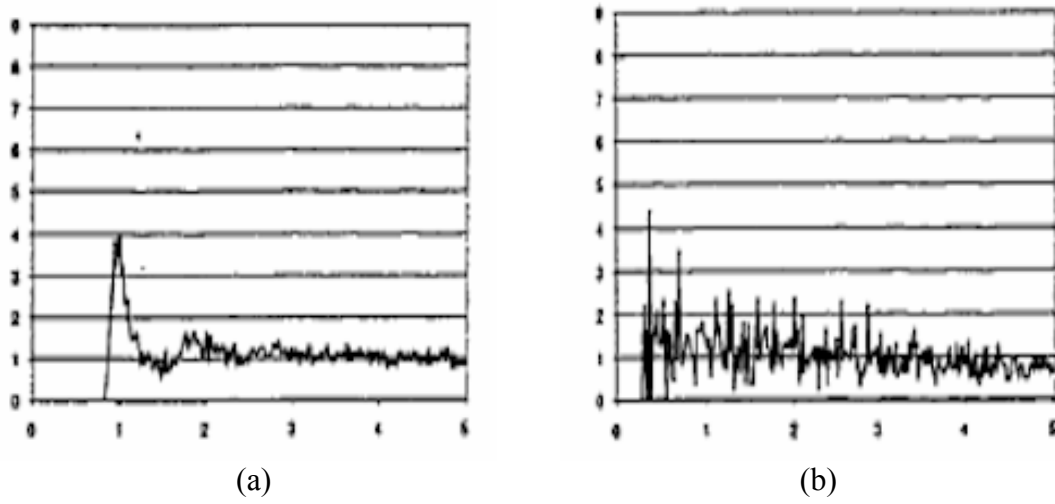


Figure 8. (a) Pair correlation function for a liquid. (b) Pair correlation function for a gas (Vasut, 2001).

is chosen, having a midpoint at r_0 and a bond angle θ_0 . The function $\cos[6(\theta_i - \theta_0)]$ is averaged for all bonds i whose midpoints lie in an annular ring of radius $r = |r_i - r_0|$ about the center point bond. The result is then averaged for all bonds acting as a center point to obtain $g_6(r)$. Figure 9 shows a graph of $g_6(r)$ for a crystal lattice displaying the relationship between nearest neighbor distance and correlation. It can easily be seen that the nearest neighbor distance increases the bond-orientation decreases. Two best fit lines show approximations for exponential and power law correlation functions (Figure 9).

In order to study complex plasmas an experimental device needed to be developed that could provide a standard environment in which to conduct research. Such a platform would need to have well defined operating limits and parameters to ensure reproducibility of experiments at independent laboratories. Chapter 3 will discuss such the research platform chosen for use in this work.

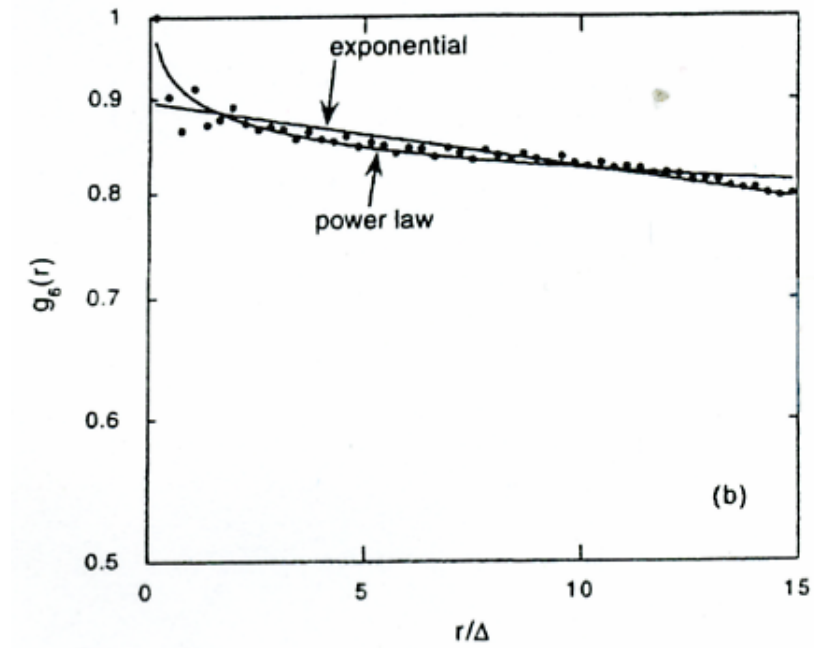


Figure 9. The bond-orientation correlation function $g_6(r)$ for the two-dimensional image in figure 5, fit by exponential and power-law decays (Pieper, 1996).

CHAPTER THREE

GEC Reference Cell and Plasma Crystals

3.1 GEC Reference Cell

To effectively study complex plasmas in a laboratory setting, the Gaseous Electronics Conference radio-frequency (GEC rf) reference cell was created in order to provide a standard for studies involving plasmas. Finalized in March 1989, the reference cell design is based on four guidelines: “ease of duplication, compatibility with a wide variety of diagnostic measurements, compatibility with the reactive gases used in plasma processing, and relevance to the discharge geometries used in the manufacture of semiconductor devices” (Hargis, 1994). This design was specified in order to provide an environment which would produce results readily reproducible in other independent reference cells (Hargis, 1994). In order to achieve identical performance at various laboratories, the electrical configuration and operating parameters were defined by comparing results from several different types of reference cells (Hargis, 1994).

As mentioned, the fundamental purpose of the GEC rf reference cell is to provide an experimental platform of common chamber geometry for the comparison of plasma measurements conducted during research by different research groups (Hargis, 1994). As such, the design of the cell is a compromise between simplicity of reference cell design and a chamber that can be used to simulate commercial applications. Capability to vary configuration and instrumentation are included in the overall design of the reference cell in order to provide a dynamic platform for researchers performing a wide range of experiments. In addition, published GEC reference cell results provide novice researchers

with guidelines on performing the basic measurements necessary to characterize rf plasmas (Hargis, 1994).

3.2 Reference Cell Design

In 1994, the construction and characterization of the GEC rf Reference Cell was outlined in a paper by Hargis, et al. The reference cell's final design (Figure 10) consisted of a stainless-steel chamber with parallel-plate electrodes spaced 2.54 centimeters apart. Gas is injected into the discharge region of the reference cell through the upper electrode and pumped out via the manifold shown in Figure 11. Each electrode is insulated from the chamber so that each electrode's voltage can be grounded, powered, biased, or allowed to float independently of the chamber while the chamber walls serve as the ground return. Standard design includes eight ports which are arranged about the main chamber to provide ease of access to the discharge region. Four 2.75 inch ports are located on the sides of the chamber with an additional two 6 inch ports located laterally where one is often used for connecting a turbomolecular pump to achieve the desired base pressure. Finally, two 8 inch ports are located on the top and bottom of the chamber to provide visual access to the area between the parallel-plate electrodes.

The reference cell was originally designed to operate between a base pressure in the range of 10^{-5} Pa with the turbomolecular pump operating at 300 liter/sec and a maximum pressure of 130 Pa. The upper electrode contained 169 equally spaced holes on concentric circles in a "showerhead" pattern to allow gas to pass into the discharge region. This provided a gas flow through the upper electrode into the main chamber and then into a pump-out chamber through a series of slots in the lower flange as illustrated in Figure 11.

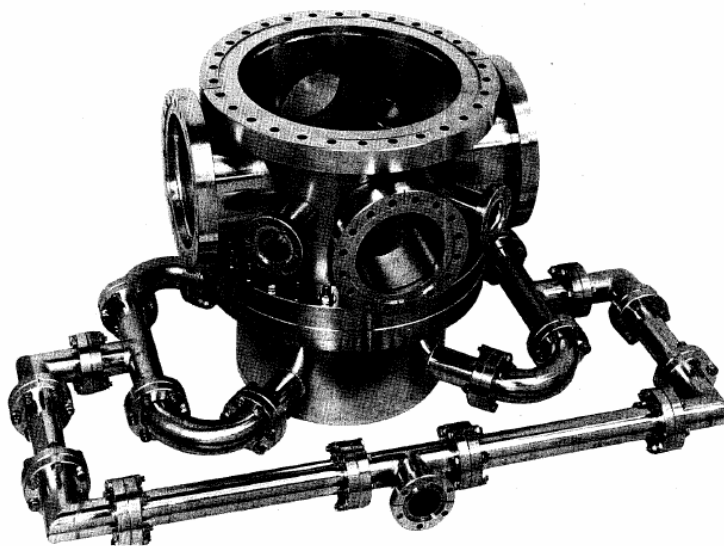


Figure 10. Photograph of main vacuum chamber of the GEC rf reference cell (Olthoff, 1995).

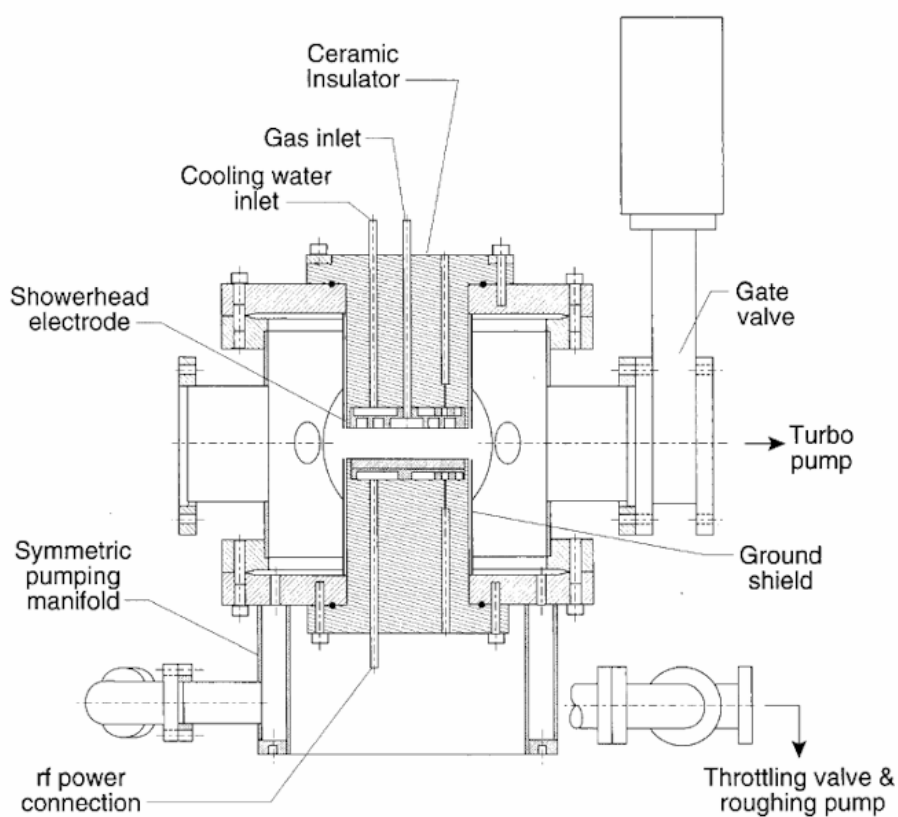


Figure 11. Schematic cross section diagram of the standard configuration of the GEC rf reference cell (Olthoff, 1995).

This design reduced azimuthal variations of gas flow characteristics. Some of the gases which have been used in a standard GEC reference cell are O_2 , SiH_4 , and Ar. Inert gases are used for three main reasons. First, inert gases allow for a more controlled experiment providing an easy mechanism for comparing the characteristics of various reference cells. Second, inert gas properties and behavior are well documented such that the benchmark characteristics of a “clean” cell can easily be documented. (A “clean” cell refers to a reference cell chamber where no dust or reactive gases have been introduced.) The known behavior of the inert gas also provides stability for theoretical model validation.

To ensure similar plasma characteristics between different chambers, identical measurements of voltage and current made for identical gases are required during initial cell configuration. The first step in this characterization is to apply a set of peak-to-peak voltages and then record the resulting wave forms. The resulting data consists of the amplitudes and phases of the first five Fourier harmonics of voltage and current, including values of the induced dc bias. This data is collected over a series of specified pressures while the cell is driven asymmetrically with one electrode powered and the other grounded. A concern in the measurement of the voltage and current of the electrode in the reference cell is the difference in measurement values from the point of measurement and the powered electrode. This difference is primarily due to the inductance between the point of measurement and the electrode and the capacitance occurring between the electrode and the ground shield. To overcome this physical obstacle an equivalent-circuit model was developed. Equivalent-circuit models may be used to calculate the voltage and current at a powered electrode based upon the measured voltage and current from a measurement point

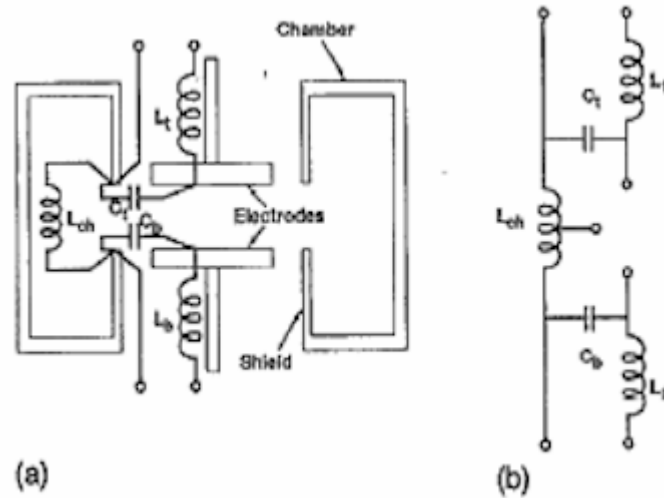


Figure 12. Schematic diagram of a GEC reference cell showing (a) the origin of the equivalent-circuit parameters and (b) the redrawn circuit. The subscripts “t” and “b” denote the top and bottom. (Hargis, 1994)

located away from the electrode. The schematic in Figure 12 shows the origin of the equivalent-circuit parameters.

As can be seen, the above circuit contains three inductors and two capacitors, creating several current paths between the plasma and the cell. Because measurements were unavailable for all the possible current paths, this circuit was not used. Instead, Figure 12(b) was simplified into Figure 13 which consists of an inductor, L , between the point of measurement and the powered electrode, and a capacitor, C , between the powered electrode and ground. The equivalent circuit below applies only for an asymmetrically driven system and is deemed adequate to compare cells at different laboratories to ensure similarity in operation. For detailed information concerning the operational and characteristic data and errors for the GEC rf reference cell, please refer to the paper by Hargis et al (1994).

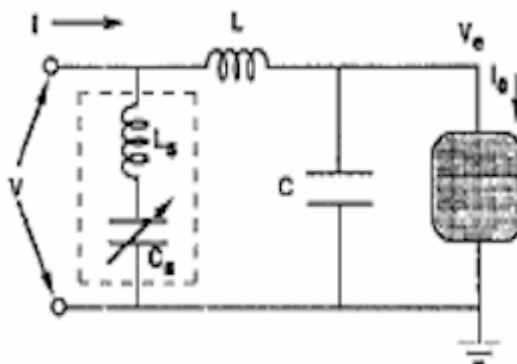


Figure 13. Simplified L-C equivalent circuit representing the reference cell. The equivalent circuit includes the components in the dashed box (Hargis, 1994).

3.3 CASPER Reference Cell

The CASPER rf reference cell was designed from the original plans codified by the GEC rf reference cell paper, but contains several important modifications. The first of these design element changes involves the electrodes. The upper electrode is a cylinder of 10.2 cm outer diameter and 9 cm inner diameter while the lower electrode is a solid cylinder 10.2 cm in diameter. Because the upper electrode is grounded, the equivalent circuit must be altered with the upper electrode no longer containing a capacitance, but instead only an inductance.

The dimensions and locations of the eight ports around the chamber remains the same although the function of some of the ports is altered. One of the 2.75 inch ports now houses the gas inlet which allows gas to enter the chamber through annular rings located in the pump-out weldment. The remaining three 2.75 inch ports provide access to the chamber for pressure gauges, Langmuir probes, etc. Two 8 inch ports, located laterally on the chamber, provide optical access to the discharge region between the electrodes. The side mounted camera uses one of the 8 inch ports while the second is used for sample

loading. Two additional 6 inch ports allow access to other additional hardware. Both 6 inch ports are used for laser illumination of the discharge region. The two 12 inch ports are located on top and bottom of the chamber to provide access to the electrodes and pump-out weldment. The top 12 inch port also provides optical access to the experimental region for the top mounted camera. The CASPER reference cell is designed to operate primarily between the pressures of 50 mTorr and 1 Torr. To operate at these pressures, one of the 6 inch ports is used for connecting a ROOTSTACK to achieve the desired vacuum. The ROOTSTACK system consists of a rotary vane pump connected directly to the chamber and a roots pump which exhausts to the outside of the reference cell. Figure 14 shows a picture of the CASPER rf reference cell.

The CASPER reference cell uses argon gas which is introduced into the system through an inlet tube mounted in one of the 2.75 inch ports. This design variation from the proposed 'showerhead' system by Hargis et al. was necessary in order to accommodate optical diagnostic tools utilizing the top 12 inch port. The gas flow rate is controlled by an external mass flow meter. The gas is then pumped out through the exhaust manifold. Gas flow characteristics are dependent upon operating pressure, but can be expected to have longer residence times at corners of the cell and vary azimuthally at lower pressures.

The introduction of dust into the chamber is accomplished through the top 12 inch port. By mounting a 5.125 inch plastic viewing port in the 12 inch flange and designing a 'shaker' for the dust, both optical access and a means for dust introduction is accomplished. The dust shaker must be filled prior to the chamber being pumped out and will accommodate and release dust up to 20 μm in diameter.



Figure 14. The top mounted camera on the CASPER rf reference cell.

3.4 Plasma Crystals

Plasma or Coulomb crystals are formed within dusty plasmas. Unlike ionic crystals which have a regular lattice structure of alternating positive and negative charges, plasma crystals generally contain all like charges in a regular lattice structure as discussed in Chapter 2. Although like charged particles tend to separate as far as possible, a lattice structure becomes the most favored stable state when an outside constraining potential is applied.

The formation of such a lattice structure of like charged particles was first theorized by Wigner in 1934. He predicted electrons would form a regular lattice due to Coulomb interactions within an electron gas in metals at low temperatures. Observation of this

condition is very difficult and experimental evidence was not found until the 1990's when several research groups reported Coulomb crystals in laboratory experiments (Chu and I, Thomas, Morfill, and Demmel, and Melzer, Trottenberg, and Piel).

Wigner crystals can only form when particles are sufficiently cool and confined in such a manner that their thermal motion will not destroy the lattice structure. Early examples of the formation of Wigner crystals were seen as colloidal suspensions of particles within an electrolytic solution. Forming crystals such as these in a laboratory setting often takes weeks and can produce optically thick structures which are difficult to successfully observe optically (Kose, 1973).

Early theoretical work within complex plasmas assumed a single type and size of dust particle embedded in plasma and confined by an external potential field (Ichimaru, 1982). It was observed that the behavior of such a system could be described by a coupling parameter, Γ , defined as the ratio of the interparticle electric energy to the average thermal energy of the particles, describing the degree in part to which a complex plasma is coupled. Where the average thermal energy is greater than the interparticle electric energy, $\Gamma < 1$ and the system is said to be weakly coupled. Systems where the interparticle electric energy dominates are characterized by $\Gamma > 1$ and said to be strongly coupled. Most naturally occurring dusty plasmas have values of Γ which are typically less than one. However, in order to create a crystalline structure of particles within the plasma such as those described previously, Γ must be much larger than one. In the majority of these cases, systems forming crystalline structures have $\Gamma > 200$ and many have Γ values that are much larger (de Angelis, 1992).

Three separate teams discovered dust crystals in 1994. One of these was located at the Max Planck Institute where a team working under the direction of Thomas, Morfill, and Goree injected $7\text{ }\mu\text{m}$ formaldehyde particles into a low temperature plasma contained within a GEC reference cell. The particles were injected through the top of the chamber and allowed to fall through the plasma acquiring an estimated charge between $9,800\text{ e}^-$ and $27,300\text{ e}^-$. The charge on the particles and the interaction with the DC self-bias of the lower electrode counteracted the gravitational force allowing the particles to float within the plasma (Thomas et. al, 1994). Employing a Γ value of $\approx 30,000$ and utilizing the equation in Chapter 2, the researchers showed that the dust was indeed in a highly ordered state (Figure 15). Observing the system from the top, horizontal dust layers were found to exist in multiple hexagonal lattices while vertical layers displayed a much less ordered structure. On average, only a few layers (Figure 16) are normally present but the research group of Zuzic et al (2000) has observed crystals with up to twenty layers where lower layers support the upper layers. Due to gravity, the system is often characterized as being “half-dimensional” so that these plasma crystals are called “two-and-one half” dimensional. The “two-and-one half” dimensional nature of the system provides problems for representing the crystal as a series of slices in the horizontal plane and then in the vertical plane. The ability of a human to do three-dimensional design is limited by both the depth-free nature of most interface devices and the inability of a human to keep track of complex three-dimensional interactions. Taking the horizontal and vertical slices and integrating them into a three dimensional representation of the original crystal shows the resulting “two-and-one half” dimensional visualization.

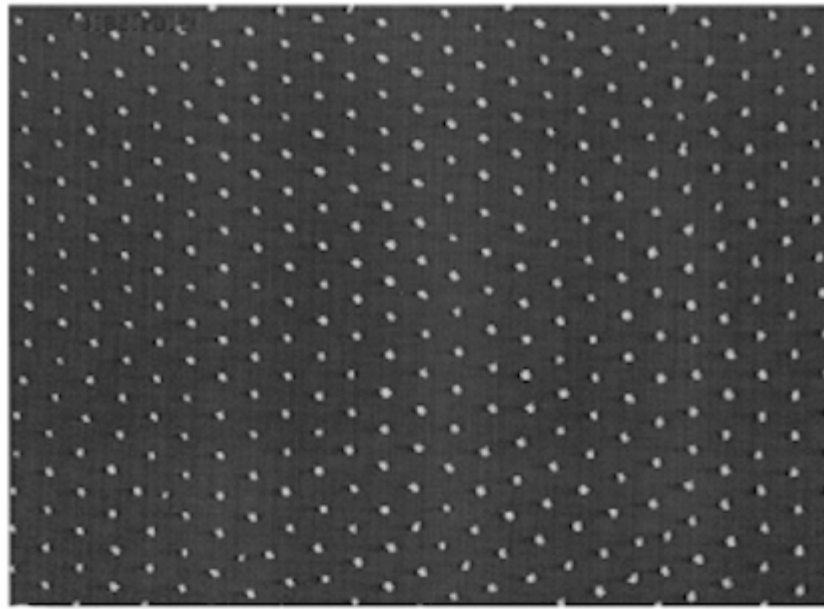


Figure 15. Horizontal lattice plane image of particle cloud displaying a two-dimensional hexagonal lattice structure (Morfill, 1996).

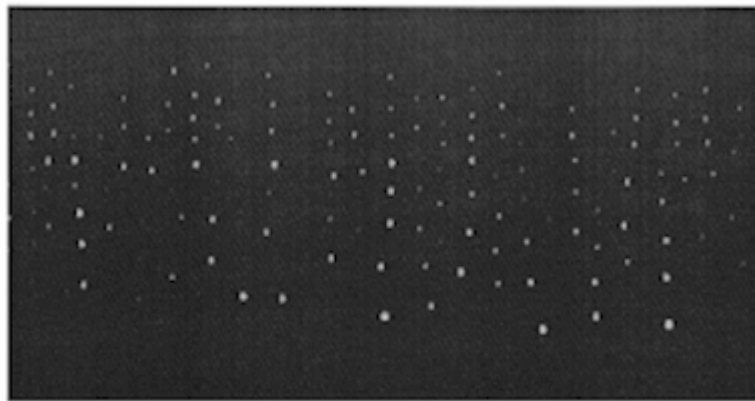


Figure 16. Vertical slice of plasma crystal demonstrating several layers of ill defined lattice structure (Morfill, 1996).

Similarly in 1994, Chu and I headed a team in Taiwan creating a Coulomb dust crystal. Although their physical apparatus differed from the Planck reference cell, the plasma parameters were similar although the method of introducing the dust was dramatically different. Instead of injecting the dust into the system, the dust was formed

by injecting O_2 and SiH_2 which formed non-uniformly sized dust particles (Chu and I, 1994). The larger particles tended to drift downward due to gravity in the constraining potential field while the smaller particles were levitated above the larger particles. As a consequence of this size distribution the bottom layers were more tightly compacted in the vertical direction than were the upper layers consisting primarily of smaller particles. The upper layers were easier to image and were observed to display the same highly ordered hexagonal structure as observed by Thomas, et al (1994) (Figure 17).

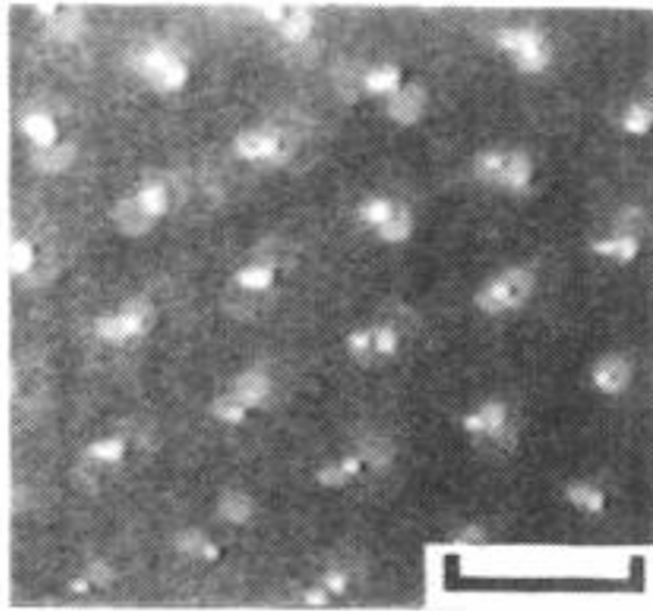


Figure 17. Horizontal slice of hexagonal lattice. Bar represents 200 μm (Chu, 1994).

The dust component of a complex plasma may vary in size from 0.1 micrometers up to 1.0 centimeters depending on whether this system being studied is an astrophysical or laboratory dusty plasma (Goertz, 1989; de Angelis, 1992). The upper limit in this range is predominately found in astrophysical dusty plasmas while the lower limit up to several microns is typical for dusty plasmas produced in a laboratory setting. Dust in the

laboratory setting may be introduced into the plasma in several ways. The most common methods are to grow the dust particles within the plasma (Chu, 1994) or to inject them into the plasma employing a “shaker” or sieve device (Cabarracas, 1996; Pieper, 1996; Thomas, 1994).

Having defined the parameters under which a rf reference cell designed to support a complex plasma would operate, a technique for data collection must now be developed. The only possible method while not altering the complex plasma within the chamber is to use some form of optical diagnostic. Chapter 4 discusses the development of such a system for the CASPER reference cell.

CHAPTER FOUR

Research and Methodology

4.1 Optical System Development

The development of a digital optical diagnostic system evolved from a need to better capture and process images of complex dusty plasmas. Past research captured analog video images on VCR recording equipment with these images then digitized on a computer and then processed by another computer system. Unknown amounts of data were lost during this digital process. The primary goal of creating a completely digital system was to eliminate this source of data loss and speed overall analysis by combining imaging and processing techniques into one concise package.

Governing factors in developing this new digital system included dimensions of the reference cell, the size of particles to be used and the estimated spacing they would have within the plasma, the estimated size of the crystal, the desired field of view and depth of field, the resolution of particles, and the image capture rate. All of these factors are crucial in determining the proper lens, camera, and illumination configuration. The camera lens and camera must be able to resolve individual dust particles from one another and still provide a large enough field of view to determine long-range ordering within the crystal. Illumination must be sufficient for the dust particles to be imaged, but not powerful enough to perturb particles within the crystal lattice.

4.1.1 Cell Dimensions

For proper analysis the entire lattice must be observed from the bottom through the top layer. In order to clearly focus and image all layers of the crystal, the dimensions of the upper and lower electrode and the electrode spacing within the reference cell was the first parameter that needed to be addressed. As mentioned in the previous chapter, the lower electrode has a diameter of 10.2 cm and is separated from the upper electrode of outer diameter 10.2 cm and inner diameter 9 cm by a distance of 2.54 cm. Thus, the dusty plasma cloud is generally confined to this volume occupying a region of approximately 4-6 cm in diameter and up to 2 cm thick.

Both top and side mounted cameras must be located outside the reference cell to eliminate perturbative effects caused by the movement of the cameras. The distance from the 12 in upper plexiglass port to the upper electrode is 9 in and to the lower electrode is 10 in. Thus, the top mounted camera lens must have a minimum working distance of 10 in. The top camera mount is designed to allow the camera to move away from the reference cell while maintaining this working distance for all layers. In addition to the working distance, the areal dimensions were to provide the upper limit for the field of view required for the top camera. In order to determine whether the dust had organized itself into a crystalline lattice within the plasma, long distance ordering needed to be observed. As a result, the ideal field of view for the top camera would be of the entire horizontal layer of the crystal. This proved to be impossible. Individual dust grains could not be observed while still allowing the entire crystal to be imaged. Instead an area that was both large enough to observe long distance ordering but small enough that a camera could image individual particles was estimated. The approximate area to be imaged was 1-1.5 cm².

Thus, the field of view required for the top camera-lens system was to have a field of view of 1-1.5 cm². The depth of field for the top camera-lens system was estimated to be up to 300 µm in order to observe vertical ordering of up to 3 layers. To determine the order of magnification required under these restrictions, the size of the CCD (Charge Coupled Device) sensor in the camera must be known as well as the desired field of view. The CCD sensor size currently in use is 2/3" which has dimensions of 8.6 mm x 6.4 mm. Thus, the desired field of view was approximately 10-12 mm square. Using the equation

$$m = \frac{l}{l'} \quad (14)$$

where l is the length of the CCD sensor and l' is the side length for the field of view, the magnification required for the desired parameters was 0.78. The lens needed to provide this level of magnification. The lens chosen for the top mounted camera was the Close Focus brand zoom lens with a variable focal length of 18-108 mm, a six to one magnification ratio, and a lens magnification doubler which produces a field of view of approximately 11 mm x 11 mm.

To determine what camera-lens configuration was required for the side mounted system, the reference cell dimensions were again needed as well as an estimated depth of field. The distance from the 8 inch side plexiglass port to the center of the electrodes is approximately 10 inches. The side mounted camera needed to be able to image individual dust grains from the far side of the electrode to the near side which required a lens with a minimum working distance of 254 mm (see Figure 18). Once again, the side camera must maintain this working distance while being moved. The thickness of the dust cloud is the primary determining factor for the field of view for the side camera with the number of horizontal layers to be observed at any one time determining the depth of field. Since the

average crystal lattice contains few layers, usually less than ten, the field of view was based on an estimated layer spacing of 20-100 μm . The desired field of view for the side mounted system was up to 2 mm x 2 mm for a camera with a 1/2" CCD sensor. Using the magnification equation given above, the required degree of primary magnification was 3.2. Unlike the top camera-lens system, the side system did not require as great a depth of field distance as only individual particles needed to be imaged. Any camera-lens combination with the ability to observe a single vertical sheet would also offer sufficient resolution to determine the number of layers present. The chosen lens for the side mounted system was the Infinity K2 Video Lens with an objective providing up to 4.0X magnification, 1.6-2.6 mm field of view, and a working distance of 140-214 mm. This lens allows for more detailed observations of individual particle positions. Additionally, external perturbative effects on the system can be observed and it can be determined if the ordered lattice crystal consists of individual particles or conglomerates.

4.1.2 Dust Cloud Parameters

Previous work in creating complex plasmas utilized dust particles that were typically 2-10 μm in diameter with an observed horizontal interparticle spacing of 128-250 μm (Pieper, 1996a; Thomas, 1994). As such, two specific diameters of approximately $6.50 \pm 0.08 \mu\text{m}$ and $8.89 \pm 0.09 \mu\text{m}$ were initially chosen for use within the CASPER system. The top mounted camera had to be able to distinguish individual particles at the proper working distance with a large enough field of view to observe long range ordering if present as discussed in the previous section. As a result, the smaller particles provided a lower field of view limit of 1 cm^2 while the larger sized particles provided the

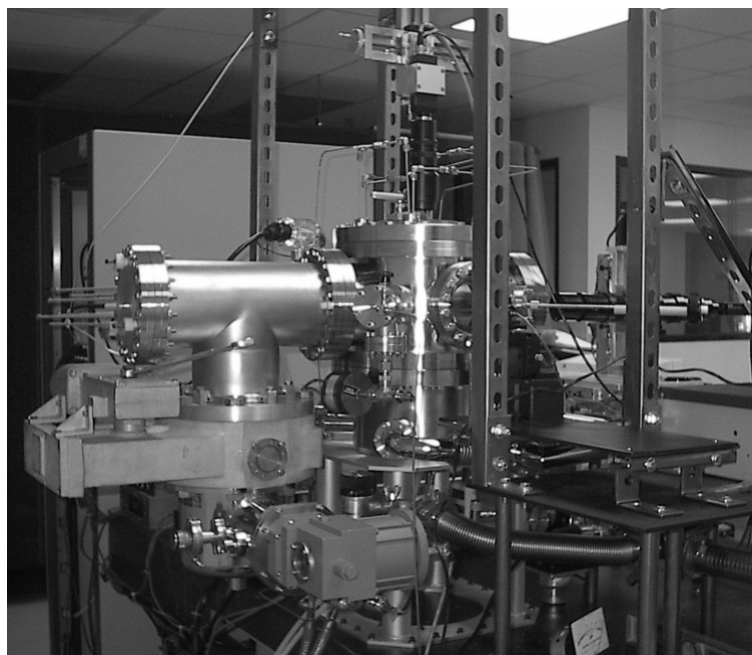


Figure 18. GEC rf reference cell and optical system consisting of two cameras mounted at right angles – one top mounted and one side mounted.

upper limit of 1.5 cm^2 . As the vertical spacing of the crystalline dust layers was expected to be approximately $20\text{-}100 \text{ }\mu\text{m}$, the side mounted camera had to have greater magnification in order to image the particles.

4.1.3 Image Capture Rate

Capturing images at a sufficient frame rate was necessary in order to track individual particles from one frame to another since any elapsed time between frames makes individual grain tracking virtually impossible. The Cohu 7800 series camera was chosen since it has the capability of collecting images at a rate of 30 frames per second with 1280×1024 pixel resolution. As images were captured by the camera, they were transmitted to the computer via a Coreco PC-RGB frame grabber board. This frame grabber has the capability of transferring images of 1600×1600 pixels from cameras at the rate of 30 frames per second. This board was chosen in part because the frame grabber

transfer rate matched the camera rate and the image size produced by the camera is smaller than the maximum size the frame grabber board can transmit.

4.1.4 Laser Illumination

In order to image the dust crystal in layers, an illumination system must be implemented. Similar to the design of the illumination system (Figure 19) of Thomas, Morfill and Demmel (1994), a Helium-Neon (HeNe) laser was located 90° to the camera and directed into the plasma discharge region through an optical port. The laser beam was fanned into a sheet using a cylindrical lens located in front of the laser and outside the chamber with the resulting planar sheet of light illuminating particles located within the sheet. A band pass filter of 612 nm was placed between the lens and camera in order to image only the particles illuminated by the laser in the fanned laser sheet. Figure 20 displays an image of a horizontally illuminated sheet of dust particles.

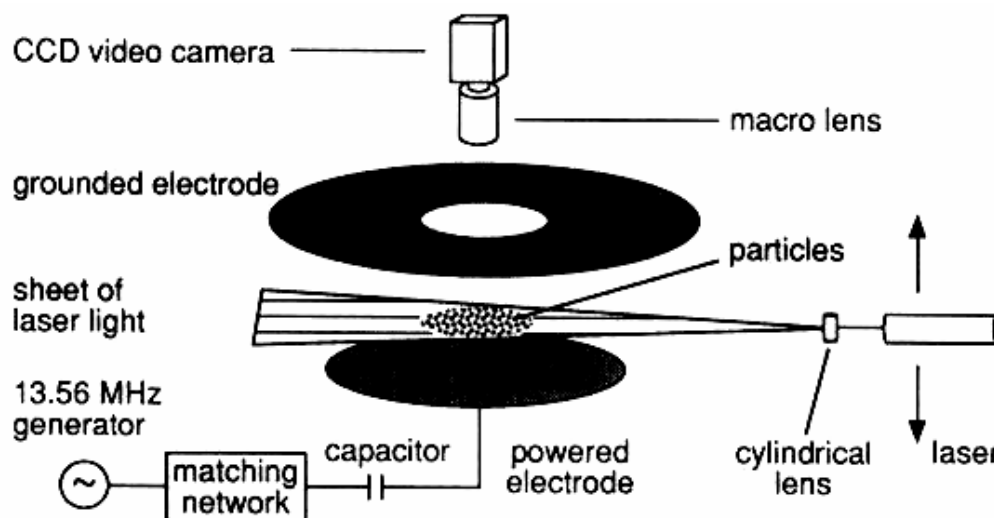


Figure 19. Schematic of laser illumination apparatus for the rf reference cell. A HeNe laser is fanned into a horizontal sheet by a cylindrical lens such that the top mounted camera may image dust particles within the laser sheet (Thomas, 1994).

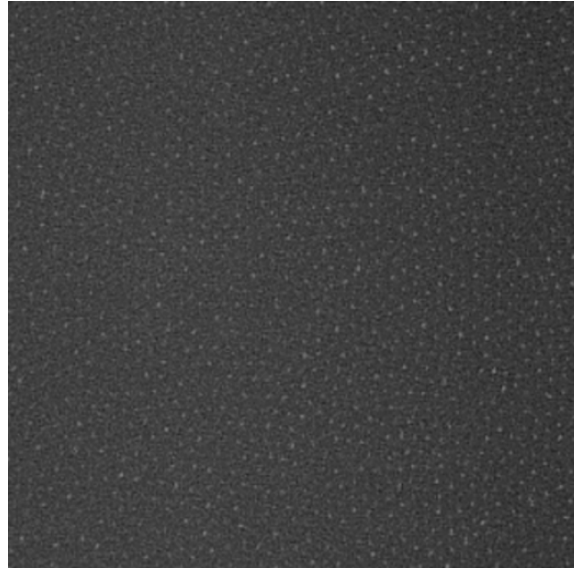


Figure 20. Raw unfiltered digital image of dusty plasma illuminated in horizontal plane.

4.2 Image Capture and Storage

It is necessary to image both horizontal and vertical cross-sections of the complex plasma in order to determine if crystalline ordering is present. To image horizontal cross-sections, the camera mounted above the chamber is focused on the horizontal Helium-Neon laser illuminated sheet. Both camera and laser sheet are then stepped incrementally from the bottom of the dust cloud to the top where each step size is $1.25\mu\text{m}$. This step size maintains the proper focal length for focused images. Vertical cross-sections are used to determine how many horizontal layers are present in any given crystal lattice, thus the side camera and laser illumination were not automated to step and image through the entire crystal.

Horizontal cross-section images determine whether or not there is long-range ordering of the particles. Multiple images must be taken in order to determine how the dust particles are moving within the plasma and at what speed, so that the average thermal energy of the complex plasma can be calculated. Twenty images were taken at each step

requiring an estimated time at each step of 0.67 seconds before moving to the next position. Assuming a crystal with a small number of horizontal layers (approximately three), an estimated maximum spacing between layers of 100 μm , a step size of 1.25 μm , and twenty images for each step, the resulting data set consists of 4,800 images. Each image occupies approximately 250 kilobytes of storage space with large data sets saved to CD in order for analysis to be performed at a later time. Images are saved as bitmap files to minimize file size and ease processing using such software as MATLAB and LABView.

4.3 Processing of Image Data

Image data is analyzed using a number of image segmentation algorithms, including both PIV (Particle Image Velocimetry) and PTV (Particle Tracking Velocimetry) techniques. Generally, PIV algorithms are used to obtain data from a densely seeded field, where individual particles cannot be easily distinguished. PTV techniques are used when the field is sparsely seeded and particles are well defined. However, PTV algorithms become inefficient when dust grains are densely situated. Tightly packed particles become difficult to identify between sequential images because the velocity of the particles may be sufficient that particles may move over half the interparticle spacing between sequential images. Essentially, when all particles in an image remain within their respective voronoi cells in sequential images, PTV techniques can be used reliably.

In the first data analysis technique, images are analyzed using an image segmentation process where image contrast is maximized (Liberzon, 2001). The image is then converted to a binary form using threshold intensities where all values below the threshold value are set to zero, resulting in a black pixel, while all pixel values above the threshold value are set to one, resulting in a white pixel as seen in Figure 21. In order to

identify individual dust grains, groups of adjacent white pixels are identified and then determined to be either valid dust grains or noise by means of a minimum pixel filter. Adjacent white pixels which meet or exceed the filter size are considered dust grains, while other pixel groupings less than the filter size are ignored and are considered noise or representations of dust in other parallel planes. A list of the positions and sizes of the dust particles is then stored in memory. From this list of particle positions the interparticle spacing and a pair correlation function (Fig. 22a) along with a Voronoi diagram can be constructed (Fig. 22b).

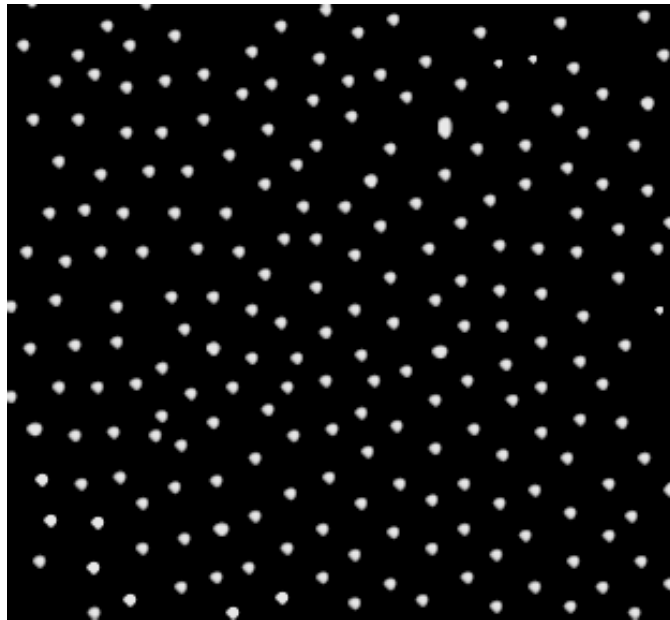


Figure 21. Black and white image of 9 μm sized dust particles in a crystalline lattice.

After the particles have been located in each image, the list of particle positions for each pair of sequential images is compared in order to detect the motion of each dust particle. This particle tracking velocimetry (PTV) technique implements a radar-type

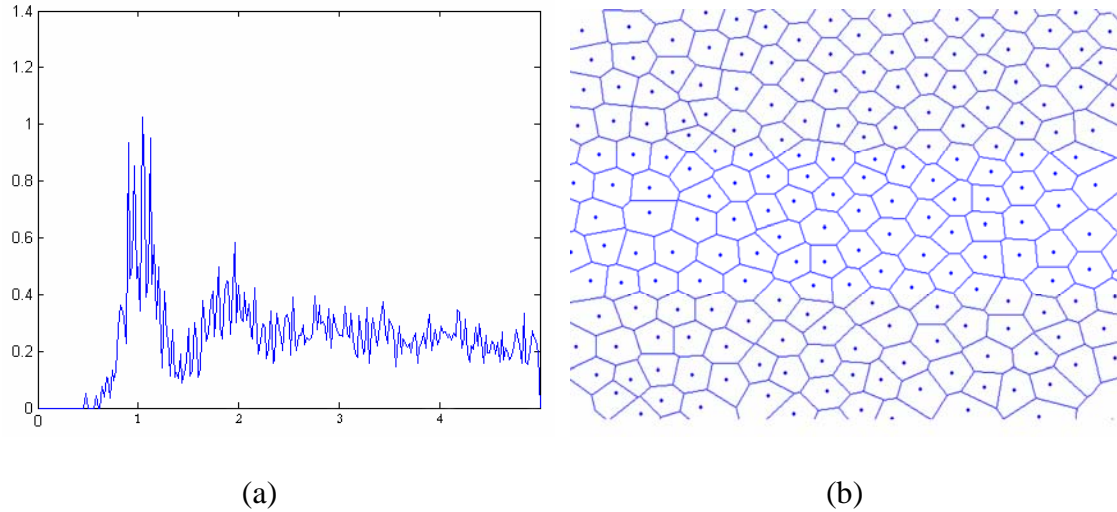


Figure 22. (a) Pair correlation function with respect to interparticle distance and subsequent (b) Voronoi diagram.

detection system to find where each particular particle is represented in the next image. Knowing the location of a particular particle in the first image, sequentially larger areas centered about that same point are examined in the second image for the particle. The search area begins with a radius of ten percent of the interparticle distance and grows by increments of ten percent until it locates a particle. If no particle is found after the search area radius has grown to fifty percent of the interparticle distance, the particle is considered lost. If two particles are found in a single search area, the one closest to the original position is chosen. When a particle is found, the system verifies by the same technique that the particle in the first image is the closest particle in that image to the particle found in the second image. By determining the distance and direction of the motion of each particle, along with the known time step between frames, the velocity information for each particle can be calculated and a PTV velocity vector plot generated, as shown in Figure 23. After confirmation of the analysis technique, the routine was applied to experimental data obtained from the CASPER GEC reference cell. Random velocities with a maximum

amplitude of 2.0 mm/sec and no propagated waves were obtained. The lack of propagated waves confirmed there was no outside source of perturbation to the plasma discharge region as set forth in the experiment design.

The PIV technique, which is a separate algorithm, does not make use of the list of particle positions or the image filtering system described above, but rather divides the image into a user-specified number of equal sized squares, or interrogation regions. Each interrogation region is then assigned a velocity vector based on the collective shift of pixel intensity in the region from one frame to the next. In this way, average velocities defined as $\bar{v} = \frac{\Delta \bar{x}}{\Delta t}$ for small groups of dust grains are calculated rather than individual particle velocities. In order to accurately use the velocity within the interrogation region the side length of the interrogation region, d , and the image magnification, s'/s are balanced against the size of the flow structures to be resolved. One way of expressing this is to require the velocity gradient to be small within the interrogation region:

$$\frac{\frac{s'}{s} \cdot |v_{\max} - v_{\min}| \cdot \Delta t}{d} < 5\% \quad (15)$$

In addition the highest measurable velocity is constrained by particles traveling further than the size of the interrogation region within some time, Δt . The result is lost correlation between the two image frames and thus loss of velocity information. As a rule of thumb:

$$\frac{\frac{s'}{s} \cdot v \cdot \Delta t}{d} < 25\% \quad (16)$$

must be true for correlation functions to be meaningful.

Since the image is not converted to binary, more noise is present, and a signal to noise limit, l , must be set. This means that when an intensity peak is found in an interrogation region, it must be at least l times the intensity of the average value of the pixels in that region in order to be considered valid. After these validation processes, PIV and PTV velocity vector plots are generated, as shown in Figure 23.

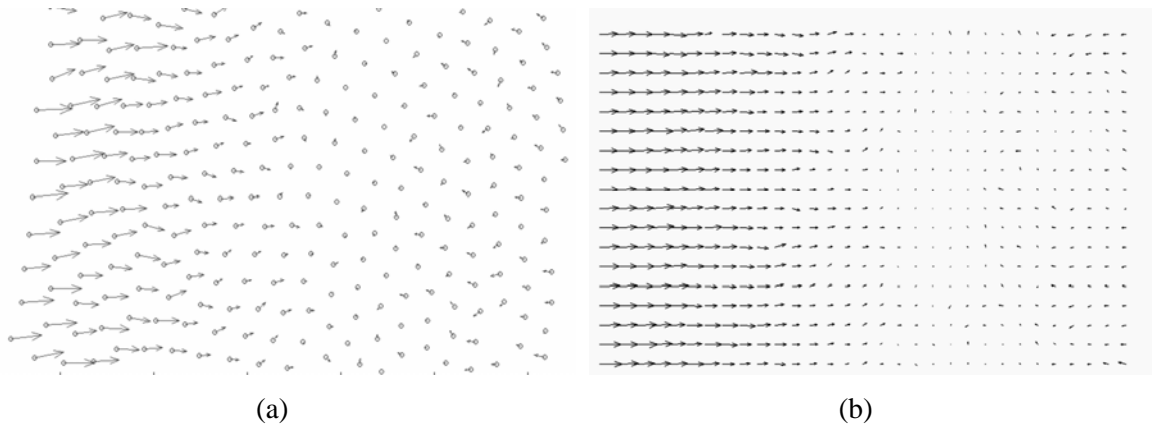


Figure 23. a) PTV velocity vector plot and b) PIV velocity vector plot.

The ability to digitally image and process the complex plasma is of vital importance in determining the extent of ordering in a complex plasma. The graphs and charts from these analysis techniques provide the basis by which complex dusty plasmas are studied in the laboratory setting.

CHAPTER FIVE

Results

5.1 Software Validation

In order to validate the analysis algorithm, an image data set with known results needed to be acquired and evaluated. If the analysis of the same image data set performed by an outside research group and the *GrainiacI* program produced similar results, then *GrainiacI* could be used for any other image data set to produce reliable results. The image data set, located at http://dusty.physics.uiowa.edu/~goree/movie_index.html, was used in the seminal paper by Thomas et al in 1994 for analysis of the crystalline structure in a Coulomb crystal. As such, it was chosen to provide the data to which the results from *GrainiacI* could be compared.

The initial collection and analysis of this image data was performed by Goree et al at the University of Iowa (Goree, 1996a and 1996b; Thomas, 1994). Image data was captured with a VHS camera and then digitized into a format suitable for computer analysis. Figure 24 shows an unprocessed image from the University of Iowa data set. This data set was processed to create a Voronoi diagram to determine ordering of the crystal lattice by calculating the number of five, six, and seven-sided cells. Figure 25 displays the Voronoi diagram where the distribution of five, six, and seven-sided cells for a small portion of the whole diagram was discovered to be approximately 20:60:17, indicating a high degree of ordering due to the majority of the cells being six-sided. No pair-correlation function was generated in the initial analysis of the data; however, a nearest neighbor chart was constructed indicating the majority of particles were within 0.2-

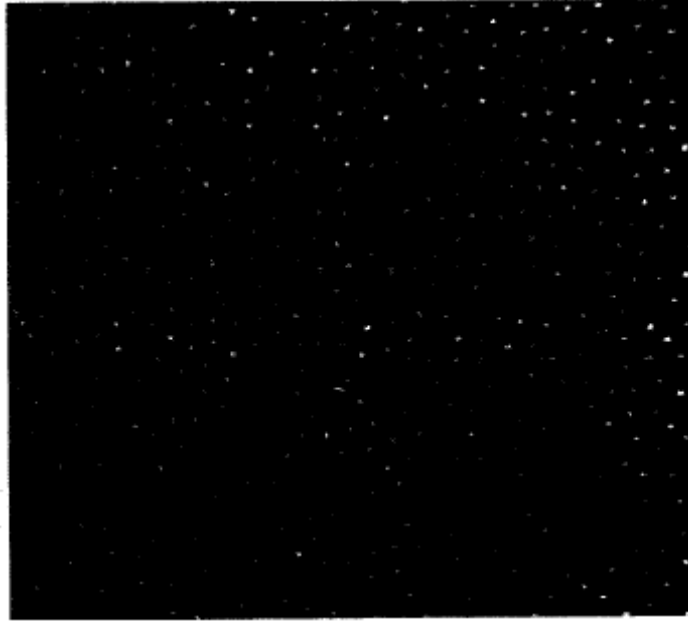


Figure 24. Image of particle cloud containing spheres with approximate diameters of $7\text{ }\mu\text{m}$ (Thomas, 1994).

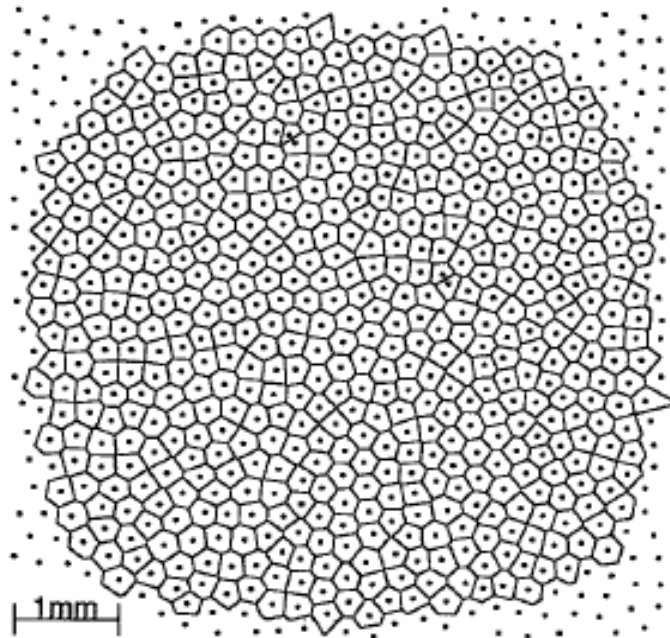


Figure 25. Voronoi diagram of the dust particles shown in Figure 24 (Thomas, 1994).

0.3 mm of one another displaying a high degree of ordering to at least the nearest neighbor (Thomas, 1994).

This same data set was processed using the MATLAB analysis program *GrainiacI*. The resulting diagrams and charts were very similar. The calculated number of particles in the raw image was 193. Figure 26 displays a Voronoi diagram constructed employing *GrainiacI* discovering a five, six, and seven-sided cell ratio of 31:136:26 compared to the original ratio of the entire original Voronoi diagram of 37:129:32. A pair-correlation function was constructed to show the nearest neighbor ordering as shown in Figure 27. Its pair-correlation function generated by *GrainiacI* displays one-well defined peak indicating a high degree of order to the nearest neighbor. Thus, these graphs validate the analysis algorithm, *GrainiacI*, by reproducing comparable results for image data collected and analyzed by an outside source.

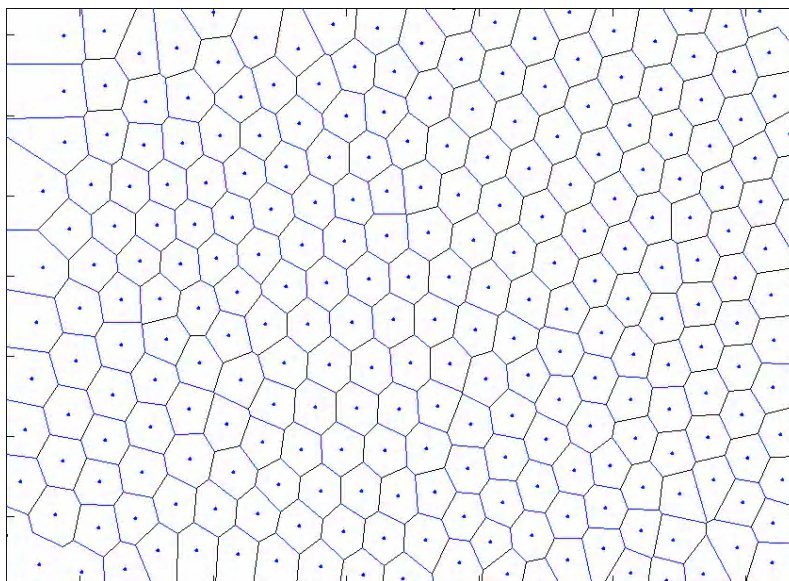


Figure 26. Portion of the Voronoi diagram constructed using *GrainiacI* for the image data shown in Figure 24.

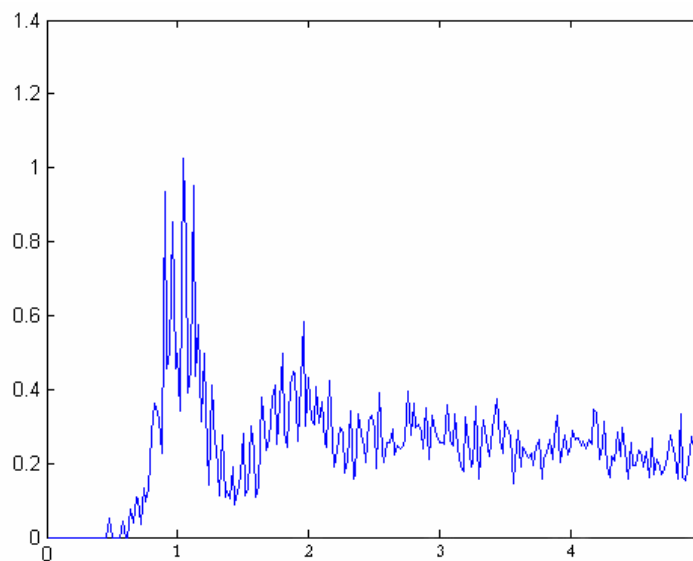


Figure 27. Pair-correlation function generated by *GrainiacI* for the image data shown in Figure 24.

5.2 Optical System Validation

To fully evaluate the optical acquisition system an image data set needed to be collected using the CASPER GEC rf reference cell. This data set would then be analyzed utilizing *GrainiacI* generating Voronoi diagrams, pair correlation functions, and two types of velocity vector plots. Preliminary analysis of image data would verify the actual magnification of dust particles and the field of view of the image plane. The information provided by Voronoi diagrams and the pair correlation function would demonstrate the amount of order in the crystalline lattice. Graphical data provided by the Matlab program would make it possible to describe the discrete velocities of the dust grains as well as the collective dynamics of the system.

Image data was collected using 9 μm diameter melamine formaldehyde particles in an Argon rf discharge. The observed magnification of the dust grains was approximately

0.75 as determined by the approximate number of particles spaced horizontally and their interparticle spacing. According to equation (14) in Chapter 4, this resulted in a field of view of 11.5 mm by 8.5 mm. This field of view was well within the desired range set forth in Chapter 4. Examining the horizontal layers of the complex plasma, individual dust grains were easily distinguishable from one another before analysis. In addition, a hexagonal lattice structure was also easily seen in the raw unprocessed image, as shown in Figure 28.

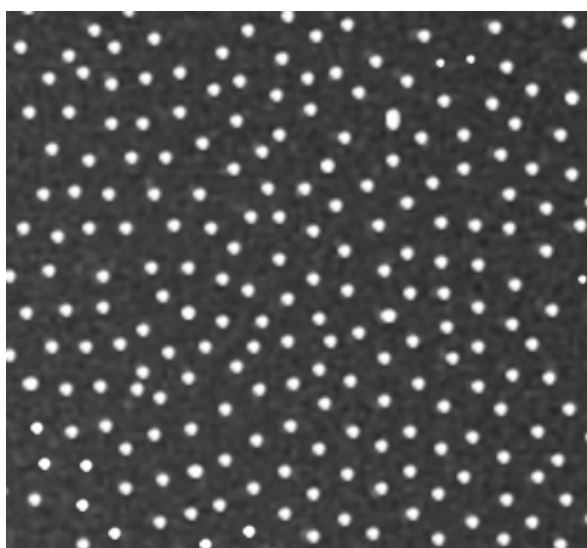


Figure 28. Raw data image showing a horizontal layer for the complex dusty plasma composed of individual 9 μ m diameter melamine formaldehyde particles and exhibiting hexagonal ordering.

As individual data sets were relatively large, an initial data analysis was performed using a limited number of data images in order to test the analysis algorithms for both PIV and PTV techniques. Using the MATLAB software package, the analysis algorithm was developed to read in the raw image data in sequential format, while allowing the user to set filter parameters, and incorporate both PIV and PTV techniques to provide a series of diagrams and plots for observing the crystalline structure formed by the dust grains

(Boessé, 2004). Both Voronoi diagrams and pair correlation functions were generated as were two types of velocity vector plots.

Once the reference cell and the CCD camera systems were operational on the GEC rf reference cell, operation parameters for the reference cell had to be established and recorded for each data collection run. For the following analysis, Table 1 shows the reference cell operating parameters under which the data used in this analysis was collected.

Table 1: CASPER GEC rf reference cell operating parameters.

Frequency	Pressure	Power	Electrode V_{rms}	I_{rms} Current	DC bias
13.56 MHz	50 mTorr	1 W	32.6 V	8.97×10^{-2} A	-23.4 V

After recording the operating parameters, 9-micron melamine formaldehyde particles were injected into the plasma where they arranged themselves into a crystalline structure. Successive images of the horizontal layers of the crystal lattice were taken with a vertical step size of $1.25 \mu\text{m}$ and then stored on CD as described in Chapter 4. For this data collection run, over six-hundred images were taken. Images at the top of the crystal were discovered to often display little usable data because few particles are located at the uppermost portions of the crystal since the lower portion of the crystal contains the majority of the dust particles and dust layers. Image data towards the middle of the collection run generally displays the most usable images for analysis as interparticle and layer spacing is relatively uniform with the majority of the particles located within this region. The images used in this analysis were numbered between three-hundred sixty and four-hundred forty of a six-hundred image collection run.

Data analysis was performed using MATLAB software and *GrainiacI*. This program incorporates both the PIV and PTV techniques as described earlier. Data analysis was divided into sets of ten images so that images within the same plane were processed together lessening the computational time. The user interface within *GrainiacI* allows the user to choose the number of images to include in each analysis run. For the aforementioned collected image data, *GrainiacI* was run with ten images per processing run for a total of eight analysis runs. The following graphs and plots were generated using images four-hundred to four-hundred nineteen of the six-hundred images collected.

During analysis, several plots are produced which describe the lattice structure in detail. The first of these is a plot of all particle positions (Figure 29). From the particle positions in each image and the time taken between frames, two different plots can be generated: a velocity vector plot and a velocity distribution plot, as seen in Figures 30 and 31. Both plots display arrows denoting the average velocity vector for each identified particle in the lattice.

A Voronoi diagram is also produced which displays the number of five, six, and seven sided cells within the overall structure. The higher the number of six-sided cells in comparison to five and seven sided cells indicates a higher degree of order within the crystalline lattice. Figure 32 is a Voronoi diagram displaying 54 five-sided cells, 127 six-sided cells, and 30 seven-sided cells. Here the high number of six-sided Wigner-Seitz cells indicates a highly ordered system of two dimensional hexagonal lattice points. The last

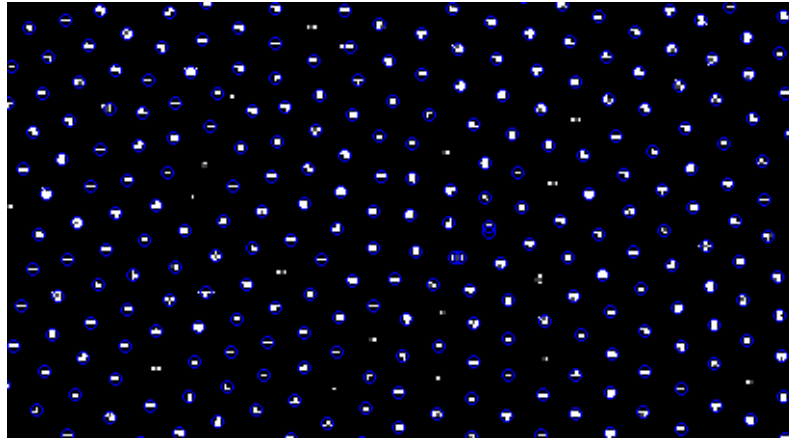


Figure 29. Particle position plot where each identified particle is located a small blue circle.

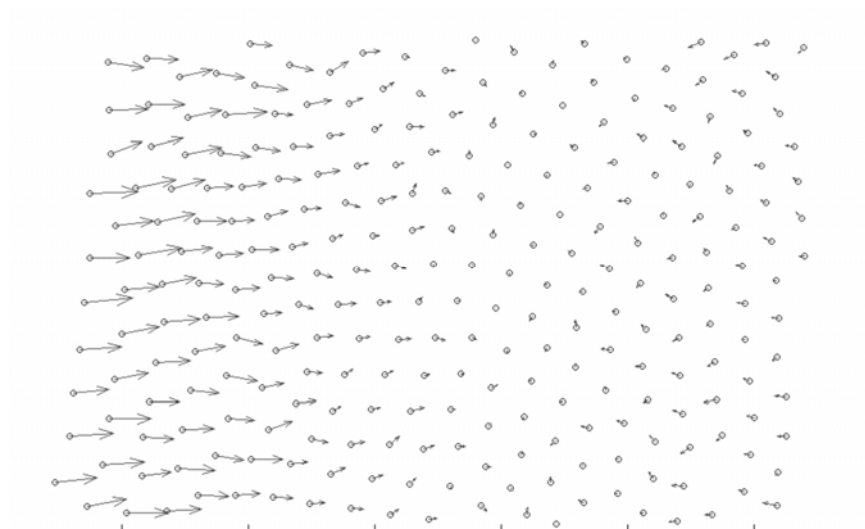


Figure 30. Velocity vector plot where circles denote particle position and arrows denote the velocity for each particle.

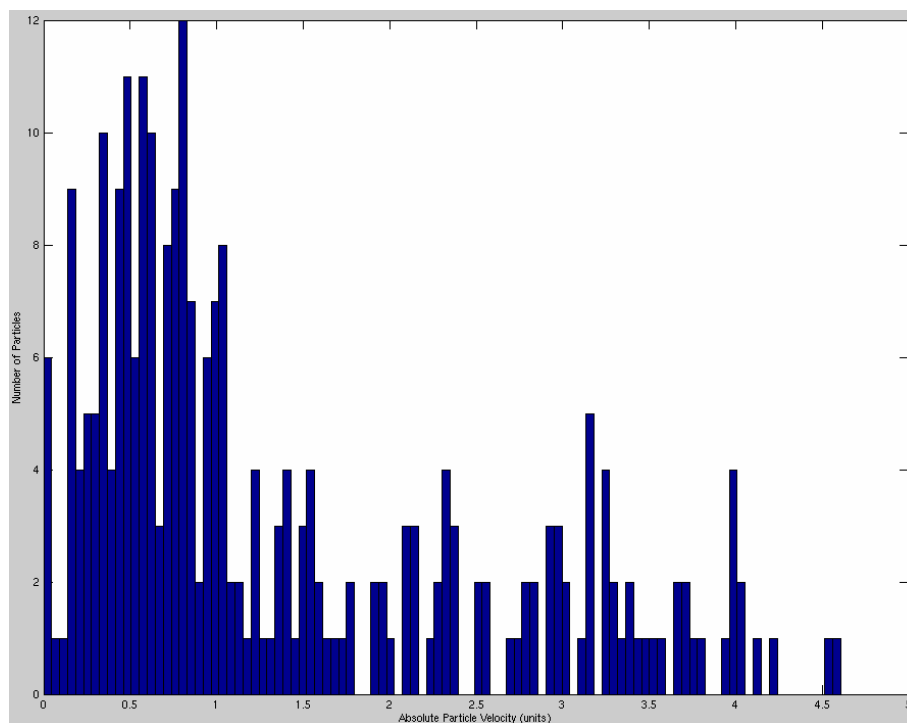


Figure 31. Velocity distribution graph.

figure shows the pair-correlation function indicating the degree to which the horizontal lattice structures is ordered. Figure 33 shows a pair correlation function where a high degree of ordering, displaying one well defined peaks and two lesser defined peaks, indicating a high degree of order for the nearest neighbor in the horizontal plane and a lesser degree of ordering for higher ordered neighbors.

In section 5.1 it was shown using image data from an outside source that comparable results to the original results could be produced validates the MATLAB software analysis program *GrainiacI*. This was a necessary step before proceeding to collect and analyze raw data from CASPER GEC rf reference cell. Earlier in section 5.2, it was shown that raw image data collected utilizing the CASPER GEC rf reference cell verifies the desired optical parameters required by this project as defined in Chapter 4.

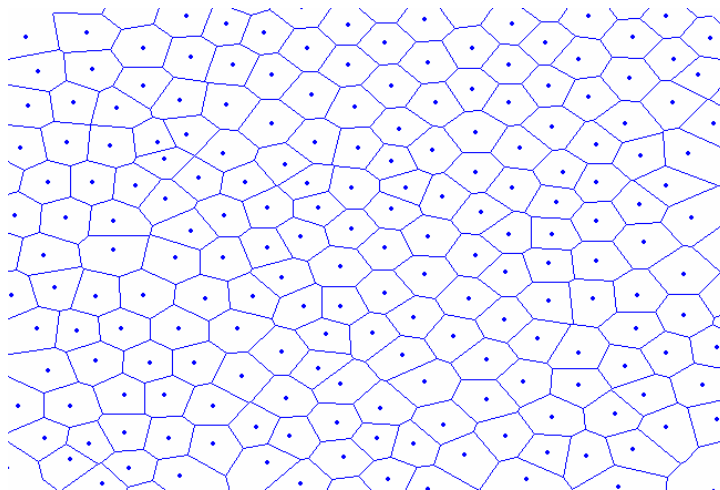


Figure 32. Voronoi diagram displaying 5, 6, and 7 sided cells with a predominance of 6 sided cells.

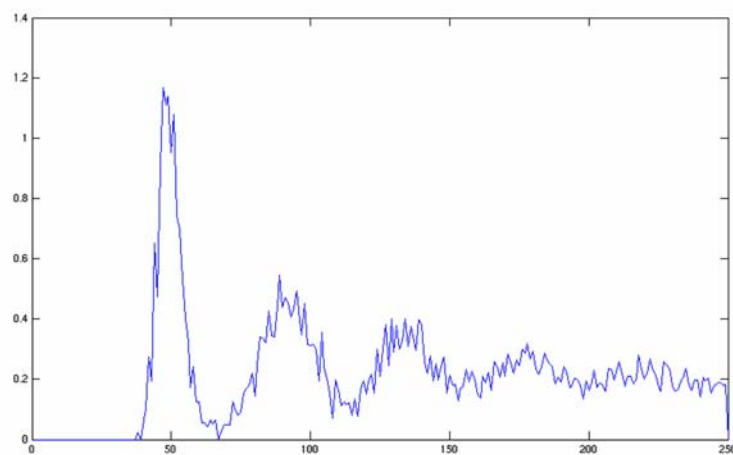


Figure 33. Pair correlation plot displaying one well defined peak indicating a well ordered lattice structure to at least the nearest neighbor.

CHAPTER SIX

Discussion and Conclusions

The development and implementation of a completely digital optical, analysis system, which minimizes the loss of data in all stages of acquisition and processing, has been completed. This system allows image data to be acquired much more quickly and efficiently than in previous analog methods. The automated camera-lens system has been shown to be successful in imaging an entire plasma discharge region at a sufficient acquisition rate with multiple images per step size to provide ease of analysis concerning position and velocity of particles and ordering of the crystal lattice. In addition, analysis techniques are also greatly improved, due primarily to uncompromised raw data with Matlab providing a user-friendly analysis tool for processing data via PIV and PTV algorithms. PIV algorithms have been shown to have the advantage of greatly reducing computation time and the ability to calculate particle velocities when individual particles are not resolvable, while PTV algorithms provide more specific information about dust grain interactions and more precise velocity calculations. The current analysis program is unique in that it can conduct both PIV and PTV techniques and be programmed to dynamically decide which algorithm is most appropriate for a certain image frame.

In future developments, a hybrid adaptive scheme should be integrated into the process, which will utilize the PIV data as a validation technique for PTV data. A second improvement to the analysis program should include a dynamic filter which selects the best threshold value for each image independently of the user so that a larger number of images can be processed more efficiently. A third improvement to the analysis algorithm could

include the development of a method to determine how many particle layers are present in the discharge region by determining the number of images for each layer and processing the layers independently of one another. Finally, data from the two cameras might be used to produce three dimensional images of the crystal lattice providing further information concerning interparticle forces and grain charging processes. Such a virtual lattice would provide a better understanding of how crystal lattices form as well as the dynamics within the crystal. As camera, optical, and computing hardware technology continues to advance, upgrades of the camera-lens system and computational power should be implemented.

APPENDIX A

APPENDIX A

```

function [] = grainiacI();
% Program name: Grainiac I
% Begin Date: 10 June 2002
% Last Edited: 23 July 2002
%
% Baylor University / Texas State Technical College
% Center for Astrophysics, Space Physics and Engineering Research (CASPER)
%
% This program is designed to be used as an optical diagnostics tool
% for dusty plasma experiments conducted in a GEC rf reference cell.
% Grainiac reads a directory containing images (format specified in ReadImDir
% function), extracts data from the images (specified in GrainData and voroData
% function), analyzes the motion of dust grains (method specified in velocity
% functions), and saves data in a .mat file.
% Develpments: In the future, this program will be updated to produce a
% report in MATLAB, and will also have more interface options.
% Functions utilized:
% setThreshValue
% setPIVvars
% read_pair_of_images
% GrainData
% voroData
% getVectors
% trackGrains
% thermEngy
% Ask for mass distribution
% GUI piv vars
% Code begins line 57
warning off      %supress warning messages
more off        %disable paging in output window
% The following four lines display a welcome graphic for 2 seconds, then 'Welcome to
GrainiacI!'
% is displayed in the Command Window
figure; run cover;
disp('Welcome to GrainiacI!');
pause(2);
close(gcf);
% In the command window, prompt the user for the full path name of the folder containing
% the images to be run. example: 'space/username/images/test1'
dirname = input('Please enter the directory name (enclose with single quotes): ');
savefile = input('Please enter the location to store data: ');

```

```

imTypeInd = input('What type of images are you running? (1=tif, 2=bmp, 3=jpg, 4=gif): ');
switch imTypeInd
case 1
    imType = 'tif';
case 2
    imType = 'bmp';
case 3
    imType = 'jpg';
case 4
    imType = 'gif';
otherwise
    imType = 'tif';
end;
[filenames,amount,filebase] = ReadImDir(dirname,imType);
% Allow the user to look at a sample image and select the lower threshold for intensities
% Select a "random" image from the middle of the sequence of images
% image = [dirname,filesep,filenames(floor(amount/2),:)];
% sample = double(imread(image))/255;
%
% [lowin, highin, lowout, highout, gamma, imgout] = intensityadjust(sample);
% thresh = setThresh(imgout);
% % The imadjust function (used in im2bw) cannot take a zero input parameter
% if thresh == 0
%     thresh = 0.01;
% end
% Allow the user to set the PIV variables. An explanation of each variable is found in
setPIVvars.
% [itt,spc,s2nm,s2nl,ips,ppm,outl,crop_vector] = varSet(BWsample);
% Override varSet until I get the GUE for varSet working
% Feel free to change these, but make sure you keep the values valid; valid values are
listed;
% ALL OF THESE MUST BE INTEGERS!!!
pRad = 3;          % expected pixel radius of an acceptable particle
itt = 25;          % valid : 1 through width of image
spc = 25;          % must be greater than 0!! and smaller than itt
s2nm = 2;          % must be either 1 or 2 (suggest 2)
s2nl = 2;          % must be greater than 1 (suggest less than 10)
ips = 30;          % must be greater than 0
ppm = 1;           % must be greater than 0
outl = 10;         % must be larger than 1 (suggest 10 or greater)
sclt = ips / ppm;  % DONT CHANGE THESE
crop_vector = [0 0 0 0];
clear image sample imgout;
% ==== Setup the Progress Bar to be used =====
info.title = 'Grainiac I Progress';
info.msg = ['Grainiac I is now processing the images in directory : ', dirname];

```

```

info.size = 4;
info.period = 0;
info.pos = 'centre';
info.color = [.34 .64 1];
info.clearance = .02;
prog = progbar(info);
% =====
se = strel('disk',pRad);
movie = []; % Create an array to hold the images as they are processed.
% Create a struct to contain data extracted from images
data = struct('grainCount', {}, 'spacing', {}, 'CMass', {}, 'BBox', {}, 'pDiff', {},...
    'absPVel', {}, 'avgVel', {}, 'tEnergy', {}, 'voroDat', {}, 'PIVectors', {}, 'PTVectors', {},
    'PCorrFxn', {});
%
% -----
% griainCount: number of images found in the image.
%   access -> data(image#).grainCount
% spacing:    average interparticle spacing in the image.
%   access -> data(image#).spacing
% CMass:      List of centers of masses of each particle found in an image
%   access x coordinate of Nth particle -> data(image#).CMass(N, 1)
%   access y coordinate of Nth particle -> data(image#).CMass(N, 2)
%   To generate a figure that plots each center of mass, execute the following command:
%       scatter(data(image#).CMass(:,1), data(image#).CMass(:,2))
% BBox:       data which constructs the smallest box which contains a particle
%   access coords. of top left corner of box for Nth particle -> data(image#).BBox(N,
1:2)
%   access horizontal width of box -> data(image#).BBox(N, 3)
%   access vertical size of box -> data(image#).BBox(N, 4)
% pDiff:      number of particles for which no representation was found in the next frame by
the PTV algorithm
%   access -> data(image#).pDiff
% absPVel:    a list of absolute velocities calculated by using the velocity vector
components
%             contained in PTVectors field
%   access the absolute velocity of the particle -> data(image#).absPVel(N)
%   where the particle's center of mass coordinates are data(image#).CMass(N, 1:2)
% avgVel:     a 2-D vector containing the average velocity of the system in an image
%             as calculated by the (1) PIV and (2) PTV algorithms
%   access PIV-calculated avg. velocity -> data(image#).avgVel(1)
%   access PTV-calculated avg. velocity -> data(image#).avgVel(2)
% tEnergy:    a 2-D vector containing the average thermal energy of the system in an
image
%             using the given mass distribution with the velocities calculated by the (1)
PIV
%             and (2) PTV algorithms
%   access PIV-calculated thermal energy -> data(image#).avgVel(1)

```

```

%    access PTV-calculated thermal energy -> data(image#).avgVel(2)
% voroDat:    contains the number of 5-sided, 6-sided, 7-sided Vigner cells
%             in a voronio diagram of the particles in the image
%    access number of 5-sided cells in an image -> data(image#).voroDat(1)
%    access number of 6-sided cells in an image -> data(image#).voroDat(2)
%    access number of 7-sided cells in an image -> data(image#).voroDat(3)
% PIVectors:  contains data obtained from PIV algorithm
%    format: data(image#).PIVectors(N,:) = [a b c d] for the Nth interrogation region,
where
%    a = x coordinate of the center of the Nth interrogation region
%    b = y coordinate of the center of the Nth interrogation region
%    c = x velocity for the particles in the Nth interrogaion region
%    y = y velocity for the particles in the Nth interrogaion region
%    to generate a velocity vector plot using this data, use the following command:
%    quiver(data(image#).PIVectors(:,1), data(image#).PIVectors(:,2), ...
%           data(image#).PIVectors(:,3), data(image#).PIVectors(:,4))
%    !!!! BE SURE to reverse the Y-Axis orientation for proper vector
representation!!!!
% PIVectors:  contains data obtained from PTV algorithm
%    format: data(image#).PIVectors(N,:) = [a b c d] for the Nth particle, where
%    a = x coordinate of the Nth particle in the first frame
%    b = y coordinate of the Nth particle in the first frame
%    c = x velocity of the Nth particle according the its position in the second frame
%    y = y velocity of the Nth particle according the its position in the second frame
%    to generate a velocity vector plot using this data, use the following command:
%    quiver(data(image#).PTVectors(:,1), data(image#).PTVectors(:,2), ...
%           data(image#).PTVectors(:,3), data(image#).PTVectors(:,4))
%    !!!! BE SURE to reverse the Y-Axis orientation for proper vector
representation!!!!
%
m = 1; %for now, set unit mass
tic
% The following for loop is iterated for each image
for fileind = 1:amount-1    % Begin Main Loop
    % Assign string variables image1 and image2 the specific file names of the
    % two images being compared in this iteration of the for loop (line 129)
    image1 = [dirname,filesep,filenames(fileind,:)];
    image2 = [dirname,filesep,filenames(fileind+1,:)];
    % image1 is read and stored as a, and image2 is read and stored as b
    [a,b] = read_pair_of_images(image1,image2,crop_vector,itt,spc);
    a = imtophat(a,se);
    b = imtophat(b,se);
    a = imadjust(a,stretchlim(a));
    b = imadjust(b,stretchlim(b));
    acceptFilter = 0;    % bool variable
    % On the first iteration, get data for the first image

```

```

if fileind == 1
    acceptCrop = 0;
    while acceptCrop ~= 1
        figure; imshow(a); set(gcf,'Name', 'Enter a crop vector in the command window');
        crop_vector = input('Please enter a crop Vector in the form [left top right bottom]:
    ');
        [m,n] = size(a);
        aCrop = a(1+crop_vector(2):m-crop_vector(4),1+crop_vector(1):n-crop_vector(3));
        figure; imshow(aCrop);set(gcf,'Name','Is this the size you want to run?');
        acceptCrop = input('Enter 1 to keep the crop vector you entered, Enter 0 to change
it: ');
    end
    a = a(1+crop_vector(2):m-crop_vector(4),1+crop_vector(1):n-crop_vector(3));
    b = b(1+crop_vector(2):m-crop_vector(4),1+crop_vector(1):n-crop_vector(3));
    while acceptFilter ~= 1
        thresh = setThresh(a);
        minArea = input('What minimum particle area would you like to use?: ');
        [data(fileind).grainCount, data(fileind).spacing, data(fileind).CMass,...
            data(fileind).BBox] = grainData(im2bw(a, thresh), minArea);
        figure; imshow(a); hold on; scatter(data(fileind).CMass(:,1),
data(fileind).CMass(:,2));
        disp(['Found ',num2str(data(fileind).grainCount),' particles']);
        acceptFilter = input('Are you happy with the filter? (Enter 1 for Yes or 0 for No):
    ');
    end
    [data(fileind).voroDat, data(fileind).PCorrFxn] = voroData(data(fileind).CMass,
data(fileind).spacing);
end %from if, 4up
acceptFilter = 0;
while acceptFilter ~= 1
    thresh = setThresh(b);
    minArea = input('What minimum particle area would you like to use?: ');
    [data(fileind+1).grainCount, data(fileind+1).spacing, data(fileind+1).CMass,...
        data(fileind+1).BBox] = grainData(im2bw(b, thresh),minArea);
    figure; imshow(b); hold on; scatter(data(fileind+1).CMass(:,1),
data(fileind+1).CMass(:,2));
    disp(['Found ',num2str(data(fileind+1).grainCount),' particles']);
    acceptFilter = input('Are you happy with the filter? (Enter 1 for Yes or 0 for No): ');
end
[data(fileind+1).voroDat, data(fileind+1).PCorrFxn] = voroData(data(fileind+1).CMass,
data(fileind+1).spacing);
% Call GrainData for the SECOND IMAGE
% Call PIV algorithm, store velocity vector plot data in appropriate field of data
data(fileind).PIVectors(:, :) = getVectors(a,b,itt,spc,s2nm,s2nl,sclt,outl,crop_vector);
% calculate average velocity and thermal energy from PIV data for current image1

```

```

[data(fileind).avgVel(1), data(fileind).tEnergy(1), junk] =
thermEngy(data(fileind).PIVectors(:,3:4), m);
% pDiff is the number of particles found not to have a representation in the second frame
[data(fileind).PTVectors(1:data(fileind).grainCount,:), data(fileind).pDiff] = ...
    trackGrains(data(fileind).grainCount, data(fileind+1).spacing, data(fileind).BBox,
...
    data(fileind).CMass, data(fileind+1).CMass, sclt);
% calculate average velocity and thermal energy from PTV data for previous image1
[data(fileind).avgVel(2), data(fileind).tEnergy(2), data(fileind).absPVel] = ...
    thermEngy(data(fileind).PTVectors(:,3:4), m);
movie(:, :, fileind) = a;          % Store image in movie array
progressbar(prog, (fileind/amount)*100); % Update progress bar
save(savefile);
end %from for fileind = 1:amount-1
movie(:, :, amount) = b; % Get the last image
% Clear the progress bar from the screen
progressbar(prog, -1);
clear prog;
% Get rid of variables we will not need again
clear a b ah bh image1 image2 fileind imTypeInd info junk;
time_elapsed = toc;
save(savefile);
run summary;
return %EOF

```

```

function [thresh, setterS] = setThreshValue(setter)
iterate = 0;
while iterate == 0
    %Show the user the image as it appears unfiltered, prompt for threshold
    sh = figure;
    set(sh, 'NumberTitle', 'off');
    set(sh, 'Name', 'Please enter lower intensity threshold (0-254) or enter (-1) for default');
    imshow(setter);
    threshR = input('\nPlease enter the lower threshold (or -1 for default value): ');
    while ~(threshR >= -1 & threshR <= 254)
        threshR = input('You entered an unacceptable value, please enter a number between -
1 and 254: ');
    end
    close(sh);
    %Set threshold
    if threshR == -1
        thresh = 240/255;          %Default value set at 240
    else
        thresh = threshR/255;
    end %From if, 4 up

```



```

setterS = imadjust(setter,[thresh 1],[0 1]);
ssh = figure;
set(ssh, 'NumberTitle', 'off');
set(ssh, 'Name', 'Are you happy with this filter? (0=No ; 1=Yes)');
imshow(setterS);
iterate = input('Are you happy with this filter? (Please enter 1 (Yes) or 0 (No)): ');
close(ssh);
end
return

```

```

function [itt,spc,s2nm,s2nl,sclt,outl,crop_vector] = setPIVvars(setter)
% setPIVvars is a function that allows the user to set the value of PIV variables:
% itt -
% spc -
% s2nm -
% s2nl -
% sclt -
% outl -
% crop_vector -
% The input parameter, setter, is a sample image from the set of images to be processed
% Prompt the user to use default settings:
default = input('Would you like to use the default PIV settings? (Yes (1) or No (0)): ');
if default == 1
    itt = 45; spc = 40; s2nm = 2; s2nl = 2; sclt = .0002; outl = 50; crop_vector = [0 0 0 0];
    return;
end
% Initialize each as null
itt = 0; spc = 0; s2nm = 0; s2nl = 0; sclt = 0; outl = 0; crop_vector = [0 0 0 0];
[x, y] = size(setter);
while ~(itt > 0 & itt <= x & itt <= y) %itt must be smaller than the image
    itt = input(['\nPlease enter the width of the interrogation areas (in pixels) \nyou would like to use, ', ...
        'or enter (-1) for help: ']);
    if itt == (-1)
        disp('HELP: The width of the interrogation area determines the size of the interrogation');
        disp('regions. Fewer particles demands a larger interrogation region. ');
    elseif ~(itt > 0 & itt <= x & itt <= y)
        disp('You entered an invalid entry. Your entry must be a positive integer');
        disp('that is smaller than either dimension of the images. ');
    end
end;

while ~(spc > 0 & spc <= itt) %spc must be smaller than itt
    spc = input(['\nPlease enter the pixel spacing of the interrogation regions \n', ...

```

```

    'or enter (-1) for help: ');
if spc == (-1)
    disp('HELP: If you enter a spacing of n, Grainiac will investigate interrogation')
    disp('regions every n pixels. If you entered an interrogation region width m');
    disp('above, then your interrogation regions will overlap by m - n pixels.');
```

```

elseif ~(spc > 0 & spc <= itt)
    disp('You entered an invalid entry. Your entry must be a positive integer');
    disp('that is smaller than the width of the interrogation regions.');
```

```

end
end;
while ~(s2nm == 1 | s2nm == 2)      %signal to noise ratio method
    s2nm = input(['\nWhich method would you like to use in calculating the signal to noise
ratio?\n', ...
    '(enter 1 for peak-by-peak search, enter 2 for peak-to-mean ratio in \none interrogation
area.): ');
    if ~(s2nm == 1 | s2nm == 2)
        disp('You entered an invalid entry. Your entry must be a 1 or 2.');
```

```

    end
end;
while ~(s2nl > 0)                  %signal to noise limit, s2n must be larger than s2nl
    s2nl = input(['\nPlease enter a signal to noise limit or enter (-1) for help: ']);
    if s2nl == (-1)
        disp('HELP: After a signal to noise ratio (s2n) has been calculated for an')
        disp('interrogation region, if s2n is smaller than the signal to noise limit,');
        disp('then the signal from that region is too weak to be processed.');
```

```

    elseif ~(spc > 0 & spc <= itt)
        disp('You entered an invalid entry. Your entry must be a positive integer.');
```

```

    end
end;
while ~(sclt > 0)                  %scaling data
    sptl = input(['\nFOR SCALING OUTPUT DATA:\n',...
    'Please enter the width of your images in meters (for scaling purposes): ']);
    fps = input('Please enter the time scale in frames per second: ');
    sclt = (sptl / x) * (fps);
end
while ~(outl > 0)                  %outltaking apart values that are bigger that OUTL times
the average value of the whole matrix.
    outl = input(['\nPlease enter an outlier filter value, or enter (-1) for help: ']);
    if outl == (-1)
        disp('HELP: The outlier filter (OUTL) is a global filter. Any velocity vectors ')
        disp('that are OUTL times the average velocity in that image are thrown out.');
```

```

    elseif ~(outl > 0)
        disp('You entered an invalid entry. Your entry must be a positive integer.');
```

```

    end
end;
%Set Crop Vector

```

```

V = figure;imshow(setter),           %Show the user a sample image
axis on,ax=axis; grid on; set(gca,'xtick',[0:itt:ax(2)],'xticklabel',[],...
    'ytick',[0:itt:ax(4)],'yticklabel',[]);
disp('')                             %Prompt user for crop vector.
crop_vector = input(sprintf('%s \n %s \t ',...
    'Enter the number of interrogation lines to crop',...
    '[Left,Top,Right,Bottom], Enter for none '));
if isempty(crop_vector),crop_vector = zeros(4,1); end
close(V);
return
%Prompt for each variable
%If the user enters ?, then a help message is printed on the screen
%Check for proper value of each variable
%itt =
%Run Sample PIV algorithm for setter image
% Argument check: s2nm must be 1 or 2, other values are assigned 2
if s2nm ~=1 & s2nm ~= 2
    s2nm = 2;
end %from if, line 2up
return

```

```

function [A,B] = read_pair_of_images(image1,image2,crop_vector,itt,spc)
% READ_PAIR_OF_IMAGES - reads two images (image1,image2) as BMP files
% and crops them according to 'crop_vector'
% This function is designed to be used with grainiac programs and urapiv
% Inputs:
%     image1,image2 - BMP file names (string)
%     crop_vector - 4 x 1 vector of following values:
%         [left,top,right,bottom] - each value is a number of lines
%         of interrogation areas (ITTxITT pixels)
%         which should be removed before the analysis.
%     itt - interrogation area size in pixels
%     spc - grid spacing (overlapping) size in pixels
% Authors: Alex Liberzon & Roi Gurka
% Date: 20-Jul-99
% Last modified: 10 July 2002
% Read the images using Image Processing Toolbox -> images are now
% matrices in MATLAB
A = double(imread(image1))/255;
B = double(imread(image2))/255;
% A = double(rgb2gray(imread(image1)))/255;
% B = double(rgb2gray(imread(image2)))/255;
% Find dimensions of the matrices A and B
[sx,sy]=size(A);[sxb,syb]=size(B);
% A & B matrices must be the same size, so we use the smallest:

```

```

sx = min(sx,sxb); sy = min(sy,syb);
% Crop the images to the desired size and make sure that there are an
% integer number of interrogation areas in the image
%
%      ---- t ---
%      |          |
%      |          |
%      l          r
%      |          |
%      |          |
%      --- b ----
%
%
l = crop_vector(1); % number of columns to cut from the left side of the image
t = crop_vector(2); % number of rows to cut from the top of the image
r = crop_vector(3); % number of columns to cut from the right side of the image
b = crop_vector(4); % number of rows to cut from the bottom of the image
% Redefine the matrices according to the crop vectors
A = A((1+t):spc*floor(sx/spc)-b,(1+l):spc*floor(sy/spc)-r);
B = B(1+t:spc*floor(sx/spc)-b,1+l:spc*floor(sy/spc)-r);
return

```

```

function [grainCount, intPartSpc, CM, Boxes] = grainData(image, minArea)
%grainData finds the number of particles in an image and the average
%space between the particles according to the eqn (area/#of grains).
%This program is designed to be used with grainiac programs
%Date: 11 June 2002
%Last modified: 11 June 2002
%Parameters:
% input: image - should be an intensity image of any dimension
%        minArea - the smallest area to be considered an object
% output: grainCount - number of objects found in image
%         intPartScp - statistical interparticle spacing of the objects
%         (optional output parameter may be added: CM - two-column
%         matrix containing coords. of centers of mass.)
%Set default parameter
if nargin == 1
    minArea = 0;
end
%Check parameter value
if ~(minArea >= 0 & minArea < 10000)
    minArea = 4;
end
%image1 = im2bw(image);
[labels, numObjects] = bwlabel(image, 8);    %Call MATLAB fxn bwlabel

```

```

graindata = regionprops(labels, 'Area', 'Centroid', 'BoundingBox');
grainCount = 0;
for i=1:numObjects
    if graindata(i).Area > minArea
        grainCount = grainCount + 1;           %Counts objects of proper size
        CM(grainCount,:) = graindata(i).Centroid; %Lists coords. for centers of mass
        Boxes(grainCount,:) = graindata(i).BoundingBox;
    end
end
%if grainCount == 0
% return
%end
[sx, sy] = size(image);
intPartSpc = sqrt((sx*sy)/grainCount); %Find interparticle spacing
return

```

```

function [data, PCorr] = voroData(CM, IPD)
% voroData is a function designed to help grainiac determine the order of
% a system of particles.
% input parameter:
% CM - a n-by-2 list of points where n is the number of points located by
% grainiac
% output parameters:
% voroData calculates the data necessary to create a voronoi diagram of the
% points provided in CM. Then, voroData calculates the number of cells in
% that diagram which have five, six, or seven sides, and returns those numbers
% in their respective variable: five, six, or seven
% Initialize each to zero
five = 0;
six = 0;
seven = 0;
% voronoi(CM(:,1),CM(:,2)) %This actually plots a voronoi diagram
% voronoin() returns two pieces of information:
% Verts - a list of all voronoi cell verticies in the voronoi diagram of
% the points listed in CM (in rows 1 through m, where there are m verticies)
% vertNums - for each cell, vertNums{cell#} lists the vertex numbers (corresponding to
% row numbers in Verts), which construct that individual cell. If vertNums{1}
% contains [2 4 11 15], then the cell surrounding point 1 has four vertices, which
% defined by the vertex locations found in the second, fourth, eleventh, and 15th
% rows of Verts.
[Verts, vertNums] = voronoin(CM);
numCells = length(vertNums); % numCells is the number of cells in the diagram
for i = 1:numCells % search each cell
    if length(vertNums{i}) == 5 % is the cell five sided?
        five = five+1;
    end
end

```

```

elseif length(vertNums{i}) == 6      % is the cell six sided?
    six = six+1;
elseif length(vertNums{i}) == 7      % is the cell seven sided?
    seven=seven+1;
end
end
data = [five, six, seven];
%
=====
%          Calculate Pair Correlation Function
=====
PCorr = [];
for i = 1:250
    PCorr(i) = 0;          % Initialize PCorr to all zeros
end
[numP, junk] = size(CM);
for i = 1:numP
    for j = i+1:numP
        dist = sqrt( ( CM(i,1) - CM(j,1) )^2 + ( CM(i,2) - CM(j,2) )^2 );
        d_int = round( 50*dist/IPD );
        if d_int < 250
            PCorr(d_int) = PCorr(d_int) + 1;
        end;
    end
end;
for i = 3:250
    PCorr(i) = PCorr(i) / ( ( i*IPD/50 + 0.5)^2 - ( i *IPD/50 - 0.5)^2 );
end
return

function [vectorList] = getVectors(a,b,itt,spc,s2nm,s2nl,sclt,outl,crop_vector);
[ sx, sy] = size(a);
% Prepare the results storage;
reslenx = floor((sx-itt)/spc+1);      % Added floor to this and next line, MKH
resleny = floor((sy-itt)/spc+1);
res = zeros(reslenx*resleny,5);
resind = 0;
a2 = zeros(itt);
b2 = zeros(itt);
Nfft = 2*itt;
c = zeros(Nfft,Nfft);
%%%%%% Start the loop for each interrogation block %%%%%%%%%
for k=1:spc:sx-itt+1
    %disp(sprintf('\n Working on %d pixels row',k))
    for m=1:spc:sy-itt+1

```

```

% Remove following line if you like 'silent' run
%fprintf(1, '.');

a2 = a(k:k+itt-1,m:m+itt-1);
b2 = b(k:k+itt-1,m:m+itt-1);
c = cross_correlate(a2,b2,Nfft);
[peak1,peak2,pixi,pixj] = find_displacement(c,s2nm);
if peak1 == peak2 & length(pixi) > 1 & length(pixj) > 1
    peakx = 0;
    peaky = 0;
    s2n=1;
else
    [peakx,peaky,s2n] = sub_pixel_velocity(c,pixi,pixj,peak1,peak2,s2nl,sclt,itt);
end
% Scale the pixel displacement to the velocity
u = (itt-peaky)*sclt;
v = (itt-peakx)*sclt;
x = m+itt/2-1;
y = k+itt/2-1;
%if peak1 == peak2
%    u = 0;
%    v = 0;
%end
resind = resind + 1;
res(resind, :) = [x y u v s2n];
end
end
no_filt_res = res;
% Reshape U and V matrices in two-dimensional grid and produce
% velocity vector in U + i*V form (real and imaginary parts):
u = reshape(res(:,3),resleny,reslenx); %4 to 3
v = reshape(res(:,4), resleny,reslenx); %3 to 4
vector = u + sqrt(-1)*v;
% Remove outliers - GLOBAL FILTERING
vector(abs(vector)>mean(abs(vector(find(vector)))))*outl) = 0;
u = real(vector);
v = imag(vector);
% Adaptive Local Median filtering
kernel = [-1 -1 -1; -1 8 -1; -1 -1 -1];
tmpv = abs(conv2(v,kernel,'same'));
tmpu = abs(conv2(u,kernel,'same'));
% WE HAVE TO DECIDE WHICH LIMIT TO USE:
% 1. Mean + 3*STD for each one separately OR
% 2. For velocity vector length (and angle)
% 3. OR OTHER.
lmtv = mean(tmpv(find(tmpv))) + 3*std(tmpv(find(tmpv)));

```

```

lmtu = mean(tmpu(find(tmpu))) + 3*std(tmpu(find(tmpu)));
u_out = find(tmpu>lmtu);
v_out = find(tmpv>lmtv);

% Let's throw the outliers out:
u(u_out) = 0; u(v_out) = 0;
v(v_out) = 0; v(u_out) = 0;
vector = u + sqrt(-1)*v;
res(:,3) = reshape(real(vector),resleny*reslenx,1);
res(:,4) = reshape(imag(vector),resleny*reslenx,1);
% Filtered results will be stored in '.._flt.txt' file
filt_res = res;
% Interpolation of the data:
[indx,indy] = find(~vector);
while ~isempty(indx)
    for z=1:length(indx)
        k = [max(3,indx(z))-2:min(resleny-2,indx(z))+2];
        m = [max(3,indy(z))-2:min(reslenx-2,indy(z))+2];
        tmpvec = vector(k,m);
        tmpvec = tmpvec(find(tmpvec));
        vector(indx(z),indy(z)) = mean(real(tmpvec))+ sqrt(-1)*mean(imag(tmpvec));
    end
    [indx,indy] = find(~vector);
end
res(:,3) = reshape(real(vector),resleny*reslenx,1);
res(:,4) = reshape(imag(vector),resleny*reslenx,1);
vectorList = res(:,1:4);
return
%EXTERNAL FUNCTIONS CALLED BY getVectors
function [c] = cross_correlate(a2,b2,Nfft)
% CROSS_CORRELATE - calculates the cross-correlation
% matrix of two interrogation areas: 'a2' and 'b2' using
% IFFT(FFT.*Conj(FFT)) method.
% Modified version of 'xcorrf.m' function from ftp.mathworks.com
% site.
% Authors: Alex Liberzon & Roi Gurka
c = zeros(Nfft,Nfft);
% Remove Mean Intensity from each image
a2 = a2 - mean2(a2);
b2 = b2 - mean2(b2);
% Rotate the second image ( = conjugate FFT)
b2 = b2(end:-1:1,end:-1:1);
% FFT of both:
ffta=fft2(a2,Nfft,Nfft);
fftb=fft2(b2,Nfft,Nfft);
% Real part of an Inverse FFT of a conjugate multiplication:

```



```

c = real(ifft2(ffta.*fftb));
return

function [peak1,peak2,pixi,pixj] = find_displacement(c,s2nm)
% FIND_DISPLACEMENT - Finds the highest peak in cross-correlation
% matrix and the second peak (or mean value) for signal-to-noise
% ratio calculation.
% Inputs:
%     c - cross-correlation matrix
%     s2nm - method (1 or 2) of S2N ratio calculation
% Outputs:
%     peak1 = highest peak
%     peak2 = second highest peak (or mean value)
%     pixi,pixj = row,column indeces of the peak1
% Authors: Alex Liberzon & Roi Gurka
% Date: 20-Jul-99
% Last modified:
% Find your majour peak = mean pixel displacement between
% two interrogation areas:
[Nfft,junk] = size(c);
peak1 = max(c(:));
[pixi,pixj]=find(c==peak1);
% Temporarily matrix without the maximum peak:
tmp = c;
tmp(pixi,pixj) = 0;
% If the peak is found on the border, we should not accept it:
if pixi==1 | pixj==1 | pixi==Nfft | pixj==Nfft
    peak2 = peak1; % we'll not accept this peak later, by means of S2N
else
    % Look for the Signal-To-Noise ratio by
    % 1. Peak detectability method: First-to-second peak ratio
    % 2. Peak-to-mean ratio - Signal-to-noise estimation
    if s2nm == 1 % First-to-second peak ratio
        % Remove 3x3 pixels neighbourhood around the peak
        tmp(pixi-1:pixi+1,pixj-1:pixj+1) = NaN;
        % Look for the second highest peak
        peak2 = max(tmp(:));
        [x2,y2] = find(tmp==peak2);
        tmp(x2,y2) = NaN;
        % Only if second peak is within the borders
        if x2 > 1 & y2 > 1 & x2 < Nfft & y2 < Nfft
            % Look for the clear (global) peak, not for a local maximum:
            while peak2 < max(max(c(x2-1:x2+1,y2-1:y2+1)))
                peak2 = max(tmp(:));
                [x2,y2] = find(tmp==peak2);
                if x2 == 1 | y2 == 1 | x2 == Nfft | y2 == Nfft

```

```

        peak2 = peak1;    % will throw this one out later
        break;
    end
    tmp(x2,y2) = NaN;
end
    % end of while
else
    % second peak on the border means "second peak doesn't
    exist"
    peak2 = peak1;
end
    % if x2 > 1 .....end
    % PEAK-TO-MEAN VALUE RATIO:
elseif s2nm == 2
    peak2 = mean2(abs(tmp));
end
    % end of second peak search, both methods.
end
    % end of if highest peak on the border
return

```

```

function [peakx,peaky,s2n] = sub_pixel_velocity(c,pixi,pixj,peak1,peak2,s2nl,sclt,itt)
% SUB_PIXEL_VELOCITY - Calculates Signal-To-Noise Ratio, fits Gaussian
% bell, find sub-pixel displacement and scales it to the real velocity
% according the the time interval and real-world-to-image-scale.
% Authors: Alex Liberzon & Roi Gurka
% Date: Jul-20-99
% Last Modified:
% If peak2 equals to zero, it means that nothing was found,
% and we'll divide by zero:
if ~peak2
    s2n = Inf;    % Just to protect from zero dividing.
else
    s2n = peak1/peak2;
end
% If Signal-To-Noise ratio is lower than the limit, "mark" it:
if s2n < s2nl
    peakx = itt;
    peaky = itt;
else
    % otherwise, calculate the velocity
    % Sub-pixel displacement definition by means of
    % Gaussian bell.
    f0 = log(c(pixi,pixj));
    f1 = log(c(pixi-1,pixj));
    f2 = log(c(pixi+1,pixj));
    peakx = pixi+ (f1-f2)/(2*f1-4*f0+2*f2);
    f0 = log(c(pixi,pixj));
    f1 = log(c(pixi,pixj-1));
    f2 = log(c(pixi,pixj+1));
    peaky = pixj+ (f1-f2)/(2*f1-4*f0+2*f2);

```

```

if ~isreal(peakx) | ~isreal(peaky)
    peakx = itt;
    peaky = itt;
end
end

```

```

function [vectors, pDiff] = trackGrains(grainCount1, IPS2, BB1, CM1, CM2, sclt)
% Could pass to trackGrains the percent of interparticle region to search
pDiff = 0;
for pInd = 1:grainCount1
    % get a range of CM's in the Bounding box of particle in frame 1
    xMin = BB1(pInd,1);
    yMin = BB1(pInd,2);
    xMax = BB1(pInd,1)+BB1(pInd,3); % Max x-coord
    yMax = BB1(pInd,2)+BB1(pInd,4); % Max y-coord
    %search CM2 for CM(x,y) in the appropriate range
    p2Ind = find(CM2(:,1)>xMin & CM2(:,1)<xMax & CM2(:,2)>yMin &
CM2(:,2)<yMax); % p2Ind is a n x 1-dim column vector
    [count, junk] = size(p2Ind);
    expand = 0;
    while expand < 5 & count < 1
        expand = expand+1;
        expLength = IPS2 * (expand/10);
        p2Ind = find( sqrt( (CM2(:,1) - CM1(pInd,1)).^2 + (CM2(:,2) - CM1(pInd,2)).^2 ) <
expLength);
        [count, junk] = size(p2Ind);
    end
    if count == 0
        p2IndList(pInd) = 0;
        pDiff = pDiff +1;
        continue;
    end
    % pick the particle that is closest: s1 is a pointer that goes down the list, s2 points to
closest
    if count > 1
        s2 = 1;
        for s1 = 2:count
            if sqrt( (CM2(p2Ind(s1),1) - CM1(pInd,1)).^2 + (CM2(p2Ind(s1),2) -
CM1(pInd,2)).^2 ) < ...
                sqrt( (CM2(p2Ind(s2),1) - CM1(pInd,1)).^2 + (CM2(p2Ind(s2),2) -
CM1(pInd,2)).^2 )
                s2 = s1;
            end
        end
        p2Ind = p2Ind(s2);
    end
end

```

```

end
% Verify that CM2(p2Ind) does not belong to another particle
verifySrch = 0; countV = 0;
while verifySrch < 10 & countV < 1
    verifySrch = verifySrch+1;
    srchRad = IPS2 * (verifySrch/10);
    vPart = find( sqrt( (CM2(p2Ind,1) - CM1(:,1)).^2 + (CM2(p2Ind,2) - CM1(:,2)).^2 )
< srchRad);
    [countV, junk] = size(vPart);
end
if countV == 0
    p2IndList(pInd) = 0;
    pDiff = pDiff +1;
    continue;
end
if countV > 1
    s2 = 1;
    for s1 = 2:countV
        if sqrt( (CM2(p2Ind,1) - CM1(vPart(s1),1)).^2 + (CM2(p2Ind,2) -
CM1(vPart(s1),2)).^2 ) < ...
            sqrt( (CM2(p2Ind,1) - CM1(vPart(s2),1)).^2 + (CM2(p2Ind,2) -
CM1(vPart(s2),2)).^2 )
            s2 = s1;
        end
    end
    vPart = vPart(s2);
end
if vPart ~= pInd
    p2IndList(pInd) = 0;
end
% Assign the index of the tracked particle to the row number of pInd
p2IndList(pInd) = p2Ind;
end
% p2IndList = verify(CM1, CM2, p2IndList);
% find displacement
for pInd = 1:grainCount1
    vectors(pInd,1:2) = CM1(pInd,:);
    if p2IndList(pInd)==0
        vectors(pInd,3:4) = [0 0];
        continue;
    end
    xDisp = CM2(p2IndList(pInd),1) - CM1(pInd,1);
    yDisp = CM2(p2IndList(pInd),2) - CM1(pInd,2);
    vectors(pInd,3:4) = [xDisp*sclt, yDisp*sclt];
end
% if there is one, get index of that CM2

```

```

    % create velocity vector [CM1(pInd,1), CM1(pInd,2), CM2(pfoundInd,1)-CM1(pInd,1),
    CM2(pfoundInd,2)-CM1(pInd,2)]
    %if there are zero, do nothing?
    % if there are more than one, which is best???
    % g = figure;
    % scatter(CM1(:,1), CM1(:,2))
    % hold on
    % scatter(CM2(:,1), CM2(:,2))
    % hold on
    % quiver(vectors(:,1), vectors(:,2), vectors(:,3), vectors(:,4));
    % set(gca,'YDir','reverse');
    % vectors is in the format of [x y u v], same as getVectors
    % CM1 is a list of centers of mass for the first image
    % CM2 is a list of centers of mass for the second image
    % how many grains are in each image
    % take thier difference
    return

```

```

function [avgVel, thermalEnergy, absoluteV] = thermEngy(velocities, mass)
% This calculates thermal energy and average velocities, given an average mass and
% a matrix of individual velocity components in the form velocities(particle #, x or y
comp)
    sq = velocities.^2;
    sqSum = sq(:,1) + sq(:,2);
    absoluteV = sqrt(sqSum);
    avgVel = mean(absoluteV);
    thermalEnergy = 0.5*mass*avgVel^2;
    return

```

BIBLIOGRAPHY

- Bliokh, P., V. Sinitsin, and V. Yaroshenko, *Dusty and Self-Gravitational Plasmas in Space*, Kluwer Academic Publishers, Boston, 1995.
- Boessé, C. M., M. K. Henry, T. W. Hyde, and L. S. Matthews, *Digital Imaging and Analysis of Dusty Plasmas*, *Advances in Space Research*, 34(11), 2374-2378, 2004.
- Bouchoule, A., *Dusty Plasmas: Physics, Chemistry and Technological Impacts in Plasma Processing*, John Wiley, New York, 1999.
- Bowers, R. L. and T. Deeming, *Astrophysics II: Interstellar Matter and Galaxies*, Jones and Bartlett, Boston, 1984.
- Chu, J. H., Ji-Bin Du, and Lin I, *Coulomb solids and low-frequency fluctuations in RF dusty plasmas*, *Journal of Physics D: Applied Physics*, 27, 296-300, 1994.
- Chu, J. H., and Lin I, *Direct Observation of Coulomb Crystals and Liquids in Strongly Coupled rf Dusty Plasmas*, *Physical Review Letters*, 72(25), 4009 (1994).
- De Angelis, U., *The Physics of Dusty Plasmas*, *Physica Scripta*, 45, 465-494, 1992.
- Fortov, V. E., A. P. Nefedov, V. A., Sinel'shchikov, A. D. Usachev, and A. V. Zobnin, *Filamentary Dusty Structures in RF inductive discharge*, *Physics Letters A*, 267, 179-183, 2000.
- Goertz, C. K., *Dusty Plasmas in the Solar System*, *Reviews of Geophysics*, 27, 271 (1989).
- Goldman, V. J., M. Santos, M. Shayegan, J. E. Cunningham, *Evidence for Two-dimensional Quantum Wigner Crystal*, *Physical Review Letters*, 65, 2189-2192, 1990.
- Hamaguchi, S., *Strongly Coupled Yukawa Plasmas-Models for Dusty Plasmas and Colloidal Suspensions*, *Plasmas and Ions*, 2, 57-68, 1999.

- Hargis, P. J., K. E. Greenberg, P. A. Miller, J. B. Gerardo, J. R. Torczynski, M. E. Riley, G. A. Hebner, J. R. Roberts, J. K. Olthoff, J. R. Whetstone, R. J. Van Brunt, M. A. Sobolewski, H. M. Anderson, M. P. Splichal, J. L. Mock, P. Bletzinger, A. Garscadden, R. A. Gottscho, G. Selwyn, M. Dalvie, J. E. Heidenreich, J. W. Butterbaugh, M. L. Brake, M. L. Passow, A. Lujan, M. E. Elta, D. B. Graves, H. H. Sawin, M. J. Kushner, J. T. Verdeyen, R. Horwath, and T. R. Turner, *The Gaseous Electronics Conference Radio-Frequency Reference Cell: A Defined Parallel-plate Radio-frequency System for Experimental and Theoretical Studies of Plasma-processing Discharges*, Review of Scientific Instruments, 65, 140-154, 1994.
- Horanyi, M., *Charged Dust Dynamics in the Solar System*, Annual Review of Astronomy and Astrophysics, 34, 383-418, 1996.
- Ichimaru, S., *Strongly Coupled Plasmas: High-density Classical Plasmas and Degenerate Electrons Liquids*, Review of Modern Physics, 54, 1017-1059, 1982.
- Ikezi, H., *Coulomb Solid of Small Particles in Plasmas*, Physics of Fluids, 29, 1764-1766, 1986.
- Jackson, J. D., *Classical Electrodynamics*, John Wiley, New York, 1975
- Jellum, G. M., J. E. Daugherty, and D. B. Graves, *Particle thermophoresis in low pressure glow discharges*, Journal of Applied Physics, 69(10), 6923-6934, 1991.
- Kose, A., *Journal of Colloid and Interface Science*, 44, 330, 1973.
- Melzer, A., T. Trottenberg, and A. Piel, *Experimental determination of the charge on dust particles forming Coulomb lattices*, Physics Letters A, 191, 301-308, 1994.
- Mendis, D. A., and M. Rosenberg, *Cosmic Dusty Plasma*, Annual Review of Astronomy and Astrophysics, 32, 98-106, 1994.
- Morfill, G. E., H. Thomas, *Plasma Crystal*, Journal of Vacuum Science and Technology A, 14(2), 490-495, 1996.
- Morfill, G. E., H. M. Thomas, U. Konopka, H. Rothermel, M. Zuzic, A. Ivlev, and J. Goree, *Condensed Plasmas Under Microgravity*, Physical Review Letters, 83, 1598-1601, 1999. [1999a]
- Morfill, G. E., H. M. Thomas, U. Konopka, and M. Zuzic, *The plasma condensation: Liquid and crystalline plasmas*, Physics of Plasmas, 6, 1769-1780, 1999. [1999b]
- Northrop, T. G., *Dusty Plasmas*, Physica Scripta, 45, 475-490, 1992.

- Olthoff, J. K., K. E. Greenberg, *The Gaseous Electronics Conference RF Reference Cell – An Introduction*, Journal of Research of the National Institute of Standards and Technology, 100, 327-339, 1995.
- Pieper, J. B., J. Goree, and R. A. Quinn, *Experimental studies of two-dimensional and three-dimensional structure in a crystallized plasma*, Journal Vacuum Science and Technology A, 14(2), 519 (1996a).
- Pieper, J. B., J. Goree, R. A. Quinn, *Three-dimensional structure in a crystallized dusty plasma*, Physical Review E, 54(5), (1996b).
- Quinn, R. A., C. Cui, J. Goree, et al., *Structural analysis of a Coulomb lattice in a dusty plasma*, Physical Review Letters, 53(3), 2049 (1996).
- Samsonov, D., and J. Goree, *Instabilities in a dusty plasma with ion drag and ionization*, Physical Review E, 59(1), 1047-1058, 1999.
- Sandford, S. A., *The Inventory of Interstellar Materials Available for the Formation of the Solar System*, Meteorites & Planetary Science, 31, 449 (1996).
- Stoffels, E., W. Stoffels, G. M. W. Kroesen, and F. J. de Hoog, *Dust in Plasmas – Fiend or Friend*, Electron Technology, 32, 255-274, 1998.
- Selwyn, G., J. E. Heidenreich, K. L. Haller, *Particle Trapping Phenomena In Radio Frequency Plasmas*, Applied Physics Letters, 57-59, 1876, 1990.
- Thomas, H., G. E. Morfill, V. Demmel, et al., *Plasma Crystal: Coulomb Crystallization in a Dusty Plasma*, Physical Review Letters, 73(5), 652 (1994).
- Vasut, J. A., *Numerical Modeling of Strongly-Coupled Dusty Plasma Systems*, Ph.D. Dissertation, Baylor University, 2001.
- Wigner, E., *On the Interaction of Electrons in Metals*, Physical Review, 46, 1002-1011, 1934.
- Zuzic, M., A. V. Ivlev, J. Goree, G. E. Morfill, H. M. Thomas, H. Rothermel, U. Konopka, R. Sütterlin, and D. D. Goldbeck, *Three-Dimensional Strongly Coupled Plasma Crystal under Gravity Conditions*, Physics Review Letters, 85, 4064-4067, 2000.